TREND AND ADVANCED STUDIES IN NATURAL SCIENCE AND MATHEMATICS

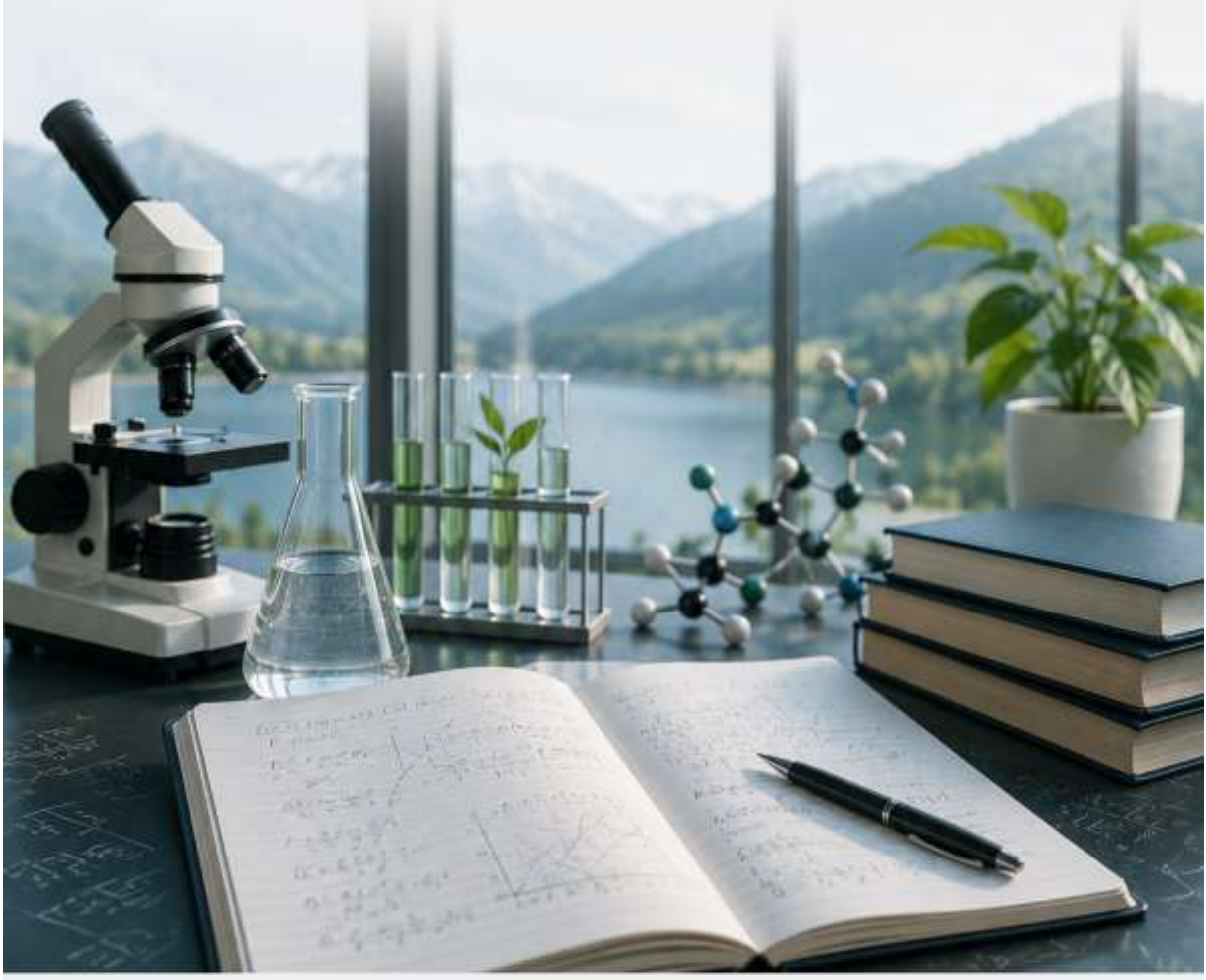

All Sciences Academy

TREND AND ADVANCED STUDIES IN NATURAL SCIENCE AND MATHEMATICS

Editor
Prof. Dr. Neslihan İYİT

Trend and Advanced Studies in Natural Science And Mathematics
Editor: Prof. Dr. Neslihan İYİT

Design: All Sciences Academy Design
Published Date: July 2026
Publisher's Certification Number: 72273
ISBN: 978-625-8839-13-5

www.allsciencesacademy.com
allsciencesacademy@gmail.com

CONTENT

Derivatization-Based Methods for the Determination of Pharmaceuticals

Ayça KARASAKAL

Prof. Dr.; Tekirdağ Namik Kemal University Science and Letters Faculty Department of Chemistry. akarasakal@nku.edu.tr ORCID No: 0000-0003-2759-4411

ABSTRACT

Derivatization is an effective analytical method in which an analyte, when it is difficult to determine directly, is converted into a form more suitable for analysis by reacting it with appropriate chemical reagents. The derivatization method is frequently used in the spectrophotometric, spectrofluorometric, and chromatographic analysis of analytes that lack sufficient chromophores or fluorophores. Derivatization enables the detection of analytes at low concentrations by increasing sensitivity and selectivity. It also reduces matrix-induced interference and improves method performance. In derivatization, analytes are converted into colored or fluorescent derivatives and analyzed using spectrophotometric and spectrofluorometric methods. There are numerous derivatization reagents available for this purpose. In this section, studies conducted using spectrophotometric and spectrofluorometric methods, which are frequently employed for the quantitative determination of pharmaceutical preparations, have been evaluated based on the current literature.

Keywords – Derivatization, NBD-Cl, NBD-F, Dansyl chloride, Fluorescamine, Fluorescein.

INTRODUCTION

Derivatization reactions improve the optical properties of analytes, leading to more accurate and reliable results in spectrophotometric, spectrofluorometric, and chromatographic analyses. Spectrofluorometric methods rely on the principle that a molecule emits fluorescence at a longer wavelength after absorbing light at a specific wavelength. However, many analytes lack intrinsic fluorescence or exhibit low fluorescence intensity. To overcome this limitation, derivatization is used to convert analytes into fluorescent derivatives, enhancing sensitivity and selectivity and enabling precise determination of analytes at low concentrations.

Various derivatization reagents—such as fluorescein, dansyl chloride, NBD-Cl, and NBD-F—are commonly used for the quantitative analysis of active pharmaceutical ingredients. These reagents are particularly effective for the derivatization of compounds containing amine, carbonyl, hydroxyl and thiol groups. Recent advances in analytical chemistry have further improved derivatization-based methods through the development of environmentally friendly reagents, microscale techniques, automated sample preparation, and chemometric data analysis. These innovations have resulted in shorter analysis times, reduced reagent consumption and greater method sustainability.

This chapter comprehensively addresses derivatization approaches used in the quantification of active pharmaceutical ingredients by

spectrophotometric and spectrofluorometric methods. It evaluates common derivatization reagents, reaction mechanisms, application areas and recent studies. Future developments and potential applications in the field are also discussed.

RESULTS AND DISCUSSION

Applications of Derivatization in Pharmaceutical Analysis

New methods were designed and validated to determine pramipexole (PRM), nebivolol (NBV), carvedilol (CRV), and eletriptan (ELT) in commercial products. The methods were based on the derivatization of drugs containing secondary amino group with NBD-Cl (7-chloro-4-nitrobenzofurazan). In this study, spectrophotometric and spectrofluorimetric methods were used. The linear range was 2.0–250 μg mL^{-1} for the spectrophotometric method and 0.1–3.0 μg mL^{-1} for the spectrofluorimetric method. The methods were optimized according to pH, volume of the reagent, temperature and reaction time. Under the optimized reaction conditions, the NBD derivatives of Pramipexole and Nebivolol exhibited maximum fluorescence emission at 529 and 530 nm following excitation at 470 and 473 nm, respectively. In contrast, the NBD derivatives of Carvedilol and Eletriptan did not show a significant fluorescence response when compared with the reagent blank. The proposed methods were successfully applied to PRM, NBV, CRV, and ELT in pharmaceutical preparations. The mean recovery values were 100.40 for PRM; 101.40 for NBV; 99.75 for CRV and 101.03 for ELT by spectrophotometric method and 100.20 for PRM; 100.28 for NBV; 101.25 for CRV and 100.21 for ELT by spectrofluorimetric method (Onal, 2011).

Almalki et al. (2024) developed a novel method for the quantification of methylphenidate hydrochloride by derivatizing with NBD-Cl in pharmaceutical preparations and human plasma. The proposed method was optimized and validated. The optimization parameters were pH, volume of NBD-Cl, solvent, temperature and reaction time. The concentration range was 2–100 ng mL^{-1}.The proposed method was successfully applied to pharmaceutical preparations and human plasma samples by using the standard addition technique. The mean recovery value was found to be 99.47% for Ritalin tablets.

A new spectrofluorimetric method was designed to determine carbamazepine in pharmaceutical preparations. Carbamazepine was derivatized with NBD-Cl. The excitation and emission wavelengths were 460 and 530 nm, respectively. The method was optimized according to pH, type of buffer, temperature, time of heating and effect of diluting solvent. The concentration range was 0.6–8.0 μg mL^{-1}. The LOD and LOQ values

were 0.06 and 0.19 μg mL^{-1}, respectively. The method was validated regarding linearity, specificity, accuracy, repeatability and precision. The proposed method was applied to analyze carbamazepine in pharmaceutical preparations. The mean recovery was found to be 100.27 % in tablets. (Walash et al.,2015).

A novel method combining spectrofluorimetry with multivariate calibration was proposed for the quantification of N-(phosphonomethyl)glycine and aminomethylphosphonic acid. The analytes were derivatized with NBD-Cl to generate fluorescent products suitable for spectrofluorimetric analysis. Fluorescence excitation–emission matrices (EEMs) were acquired by scanning excitation wavelengths from 400 to 500 nm while recording emission spectra between 500 and 610 nm. Second-order fluorescence data were analyzed using the Multivariate Curve Resolution with Alternating Least Squares (MCR-ALS) algorithm, enabling the simultaneous quantification of glyphosate and AMPA. The proposed method was successfully validated using samples containing different analyte concentrations and was further applied to the analysis of a commercial herbicide formulation and environmental water collected from an agricultural area. To compensate for potential matrix effects, the standard addition technique was employed. The established working concentration range was found to be appropriate for determining glyphosate and AMPA levels typically encountered in surface waters from soybean cultivation regions under direct seeding practices (Pérez et al.,2019).

A new analytical method was designed to quantify nateglinide in pharmaceutical preparations using a spectrofluorometric technique, based on its derivatization with NBD-Cl in borate buffer at pH 10. The excitation and emission wavelengths were found to be 464 and 537 nm, respectively. The analytical performance of the method was validated by assessing parameters including linearity, limits of detection and quantification, accuracy, precision (intra-day and inter-day), and recovery. The concentration range was 50–500 ng mL^{-1}. The LOD and LOQ were determined to be 15.14 and 45.42 ng mL^{-1}, respectively. The validated procedure was successfully applied to pharmaceutical preparations. The recovery value was found to be 99.1% in pharmaceutical preparations (Karasakal & Ulu Tatar, 2014).

An analytical spectrofluorimetric method was designed and validated to evaluate tranexamic acid in pharmaceutical preparations and spiked human plasma. The method was based on the formation of a fluorescent derivative resulting from the reaction of the primary amino group of tranexamic acid with fluorescamine. The excitation and emission wavelengths were 392 and 473.5 nm, respectively. The developed method was optimized according to reaction time,volume of fluorescamine and diluting solvent. The linear range was 0.1–0.9 μg mL^{-1}. The values of LOD and LOQ were 0.0237 and 0.0719 μg mL^{-1}, respectively. The validated method was successfully applied for the determination of tranexamic acid in

tablet and ampoule formulations, as well as in spiked human plasma samples, providing satisfactory recovery values with a mean recovery of 99.43 ± 0.62%.(Omar et al.,2021).

An ultrasensitive, rapid, simple, and cost-effective spectrofluorimetric method was developed and validated for the quantitative determination of ceftazidime pentahydrate (CEF) and vancomycin hydrochloride (VAN) in human plasma and pharmaceutical formulations. The method was based on the derivatization of the primary amino groups present in CEF and VAN with fluorescamine, producing highly fluorescent derivatives suitable for quantitative analysis. Under optimized experimental conditions, the concentration ranges were 30–300 ng mL^{-1} for CEF and 0.5–30 ng mL^{-1} for VAN. The method was applied to pharmaceutical preparations and human plasma samples. The mean recoveries were found to be 101.55 ± 0.55% for CEF and 101.85 ± 0.71% for VAN in pharmaceutical preparations. The mean recovery percentages ranged from 95.90% to 98.40% in human plasma samples (Marzouq et al.,2019).

A new analytical method was designed to analyze primaquine (PQ) in pharmaceutical preparations. The method was based on the derivatization of primaquine with fluorescamine under alkaline conditions. The excitation and emission wavelengths were 397 and 480 nm, respectively.The developed method was optimized according to pH, reaction time, temperature, and fluorescamine concentration. The linear range was 0.25–1.25 μg mL^{-1}. The values of LOD and LOQ were calculated to be 0.051 μg mL^{-1} and 0.154 μg mL^{-1} , respectively. The method also showed satisfactory accuracy, with recovery values ranging from 95% to 106%, confirming its suitability for routine quality control analysis of primaquine tablets (Altigani et al.,2018).

A novel spectrofluorimetric method was proposed to quantify famciclovir. The method was based on the derivatization of famciclovir with fluorescein. The designed method was optimized and validated according to linearity, limits of detection and quantification, precision, accuracy, recovery, and robustness. The linear range was 100–1000 ng mL^{-1}. LOD and LOQ values were 51.13 ng mL^{-1} and 153.39 ng mL^{-1}, respectively. The equation of the calibration curve was $y = 0.9383x + 62.878$. The validated method was successfully applied to the analysis of famciclovir in both its pure form and commercial pharmaceutical preparations. Recovery experiments were conducted using standard addition method and The mean recovery value was 94.77% in tablet preparations (Karasakal et al.,2015).

A new spectrofluorometric method was developed by derivatizing favipiravir with 4-fluoro-7-nitrobenzo-2-oxa-1,3-diazole (NBD-F) in the presence of its acid-induced degradation product. The degradation product formed under acidic conditions was structurally characterized using infrared (IR) spectroscopy, ^1H NMR, and mass spectrometry, confirming the hydrolysis of the amide group to the corresponding carboxylic acid derivative. The selectivity of the method was attributed to the ability of

favipiravir's primary amide group to react with NBD-F via nucleophilic substitution. The excitation and emission wavelengths were 472 and 530 nm, respectively, whereas the degradation product did not participate in the reaction. Experimental conditions were systematically optimized, and optimum derivatization was achieved using pH 8.0 borate buffer, 1.5 mL of 0.2% NBD-F, and heating at 70 °C for 25 min. The concentration range was 0.01–0.25 μg mL^{-1}. The values of LOD and LOQ were 0.0028 μg mL^{-1} and 0.0094 μg mL^{-1}, respectively. The proposed method was successfully applied to the analysis of pharmaceutical formulations and human plasma samples. The average recovery value from tablet analyses was found to be 99.22% ± 1.357. This value confirmed the absence of matrix interference caused by tablet excipients and validated the method's applicability to pharmaceutical quality control. The mean recovery value from plasma samples was found to be 99.24% ± 0.509. (Nassar et al.,2026).

A novel microwell-based photometric and spectrofluorimetric analytical approach was developed and validated to determine plazomicin (PLZ) in pharmaceutical preparations. NBD-F was used as the derivatizing reagent. The method was optimized according to NBD-F concentration, buffer solution and pH, temperature and reaction time, HCl concentration. The excitation and emission wavelengths were 473 and 541 nm, respectively. The concentration range was 20–800 μg mL^{-1} for photometric method, the linear range was between 0.05 and 1.5 μg mL^{-1} for spectrofluorimetric method. The method was successfully applied to the determination of PLZ in injectable solutions. The recovery values ranged from 98.3 to 102.1% for PLZ drug substance, and from 98.6 to 102.3% for injectable preparations. In addition, greenness evaluation confirmed that the developed methods complied with the principles of green analytical chemistry. (Alkathiri et al.,2024).

A new spectrofluorometric method based on the derivatization of ranitidine with NBD-F in pharmaceutical preparations was developed and validated. The excitation and emission wavelengths were 458 and 521 nm, respectively . The concentration range was 40–1200 ng mL^{-1}.The developed method was optimized according to volume of NBD-F, pH, temperature and time, diluting solvent and hydrochloric acid. The LOD and LOQ were found to be 0.04 and 0.12 ng/mL, respectively. Standard addition method was used for the determination of RAN in tablets. The recovery values were between 98.97 and 99.43% (Ulu Tatar& Cakar, 2012).

A novel spectrofluorimetric method was designed and validated to determine etodolac and diclofenac sodium in pharmaceutical formulations. The method was based on the derivatization reaction of both drugs with NBD-F, a selective fluorogenic reagent for primary and secondary aliphatic amines, under buffered conditions at pH 8.5. This reaction resulted in the formation of yellow-colored fluorescent derivatives suitable for quantitative analysis. The method was optimized with respect to pH, solvent, temperature

and reaction time, volume of NBD-F. The calibration range was 40–600 ng mL^{-1} for etodolac and 25–500 ng mL^{-1} for diclofenac sodium. The calculated detection limits were 0.071 ng mL^{-1} for etodolac and 0.055 ng mL^{-1} for diclofenac sodium, demonstrating the high sensitivity of the proposed method. The method was successfully applied to etodolac and diclofenac sodium in commercial preparations. The mean recovery values were 101.2±0.6% for etodolac and 99.4±0.4 % for diclofenac sodium. (Ulu Tatar, 2011)

A new chiral HPLC method was proposed for the simultaneous determination of D- and L-serine in rat brain microdialysis samples. The analytical procedure involved pre-column derivatization of both enantiomers with NBD-F, followed by chromatographic separation of the resulting fluorescent derivatives. The excitation and emission wavelengths were 470 and 540 nm, respectively. The developed method enabled clear detection of both serine enantiomers in rat brain microdialysis samples, and validation results confirmed its reliability, with acceptable precision and accuracy values within 5.14% and 109%, respectively. The method was subsequently applied to investigate the temporal changes in D-serine levels in the rat prefrontal cortex following intraperitoneal administration of D-serine. The results demonstrated the rapid distribution of D-serine into the brain extracellular fluid, followed by a gradual decline over time. This HPLC-fluorescence method provides a useful analytical tool for in vivo investigations of D-serine, an important co-agonist of the N-methyl-D-aspartate (NMDA) receptor, in the extracellular environment of the rat brain (Fukushima et al.,2004).

A sensitive spectrofluorimetric method was developed to quantify ticagrelor (TCG) in pharmaceutical formulations and human plasma. 5-(Dimethylamino)naphthalene-1-sulfonyl chloride (dansyl chloride) was used as the fluorescent derivatizing reagent. The method was based on the reaction of the secondary amino group present in ticagrelor with dansyl chloride in the presence of solution of 0.5 M sodium bicarbonate (pH 10), resulting in the formation of a highly fluorescent derivative. The experimental parameters affecting the reaction between TCG and dansyl chloride were investigated and optimized with respect to the solvent, pH, dansyl chloride concentration, buffer solution, temperature and reaction time. The excitation and emission wavelengths were 340 and 445 nm, respectively. Experimental factors influencing the derivatization reaction and fluorescence intensity were systematically investigated and optimized to achieve maximum sensitivity. The proposed method was validated, including evaluation of linearity, sensitivity, accuracy, and precision. The calibration range was 20,0–200,0 ng mL^{-1}. The values of LOD and LOQ were 0.14 ng mL^{-1} and 0.46 ng mL^{-1}, respectively. The designed method was applied to determine TCG in pharmaceutical preparations and human plasma samples. The results of the recovery studies analyzed using standard

addition method were found to be 100.27% in tablet preparations.(Onal & Kepekci Tekeli, 2020).

A novel method was designed to determine tolterodine (TOL) in pharmaceutical preparations and human plasma using a spectrofluorimetric method. The method was based on the derivatization reaction of TOL with dansyl chloride in bicarbonate buffer solution (pH 9.5).The method was optimized with respect to solvent, pH, dansyl chloride concentration, buffer solution, pH, temperature and reaction time and was validated. The wavelengths of excitation and emission were 360 and 590 nm, respectively. The concentration range was 5–60 ng mL^{-1}. The values of LOD and LOQ were 0.136 and 0.434 ng mL^{-1}, respectively. The proposed method was applied to pharmaceutical preparations and human plasma samples using the standard addition method. The recovery results were 100.5 % for tablets and 75.23-80.01 % for human plasma samples (Tekeli, 2017).

A new analytical method was developed to determine bupropion hydrochloride, fluoxetine hydrochloride, sertraline hydrochloride, amineptine hydrochloride and paroxetine hydrochloride in pharmaceutical preparations and biological fluids. Dansyl chloride was used as a derivatization agent. The wavelengths of excitation and emission were 347 and 450nm, respectively. The concentration range was between 0.02 and 0.14 μg mL^{-1}. The validated method was successfully applied to the analysis of the investigated antidepressants in pharmaceutical dosage forms and human plasma samples. The mean recovery values were 99.49–100.67 ± 0.98–1.09% for pharmaceutical preparations and 97.44–101.61 ± 0.425–1.78% for human plasma samples (Omar et al.,2014).

A new spectrofluorometric method based on the derivatization of cinacalcet hydrochloride with dansyl chloride was designed and validated. The method was optimized and validated. The concentration range was 60.0–1500.0 ng mL^{-1} .The LOD and LOQ values were 18.17 ng mL^{-1} and 55.07 ng mL^{-1}, respectively. The quantum yield of the developed method was also evaluated, and a sustainability assessment was conducted using green analytical chemistry evaluation tools. The proposed method demonstrated higher overall sustainability scores (87.2% vs. 81.7%), greater practical applicability according to BAGI scores (70.0 vs. 60.0), and better environmental friendliness according to the Green Certificate (86 vs. 73). The AGREE assessment revealed that the method is environmentally friendly, scoring 0.80 compared to the traditional approach's 0.74 (Hamad et al.,2025).

A new analytical method was proposed and validated to determine cilazapril in biological fluids and tablets. The method was based on the derivatization of cilazapril with dansyl chloride as a fluorogenic reagent. The wavelengths of excitation and emission were 374 and 503 nm, respectively. The concentration ranges were 100–500 ng mL^{-1} for plasma samples and 50–250 ng mL^{-1} for urine samples. The developed method was successfully

applied to the analysis of cilazapril in bulk drug material, pharmaceutical preparations, and biological samples, demonstrating its suitability for pharmaceutical and bioanalytical applications The mean recoveries were 84.3% for urine samples and 88.4% for tablets (Karasakal, 2015).

A novel method was designed to evaluate alfuzosin in pharmaceutical formulations and urine samples. The proposed method was based on the derivatization reaction between alfuzosin and dansyl chloride in carbonate buffer medium at pH 9.7, resulting in the formation of a highly fluorescent derivative. The wavelengths of excitation and emission were 516 and 405 nm, respectively. The analytical procedure was validated by evaluating several parameters, including linearity, limit of detection, limit of quantification, precision, accuracy, recovery, and robustness, according to established analytical method validation criteria. The calibration range was 25–500 ng mL^{-1}. The LOD and LOQ values were 8 ng mL^{-1} and 25 ng mL^{-1}, respectively. The validated method was applied to quantify alfuzosin in commercial pharmaceutical preparations and urine samples. The mean recovery values were 99.7% for tablets and 88.9% for urine samples (Karasakal & Ulu Tatar,2015).

A new method was designed to analyze tamsulosin in biological fluids and pharmaceutical preparations. Dansyl chloride was used as a derivatization agent. The method was optimized with respect to solvent, pH, dansyl chloride. The method was based on the derivatization of tamsulosin with dansyl chloride. The linearity range was between 1.22×10^{-7} and 7.35×10^{-6} M. The values of LOD and LOQ were 1.07×10^{-7} M and 3.23×10^{-7} M, respectively. The method was applied to quantify of tamsulosin in pharmaceutical preparations and urine samples. The mean recoveries were 97.19% for urine samples and 98.69% for capsules. Intraday accuracy ranged between 0.21 and 2.0%, and interday accuracy range between 0.18 and 2.03% (Karasakal & Ulu Tatar,2014).

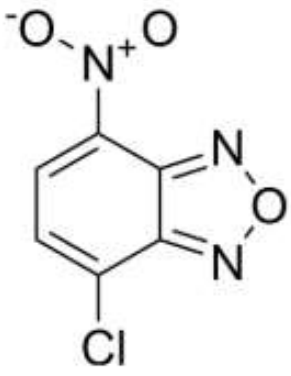

a

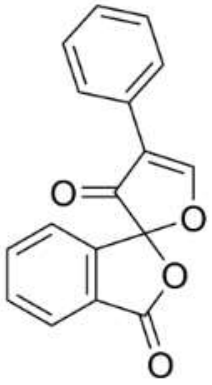

b

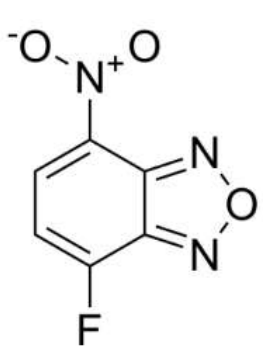

c

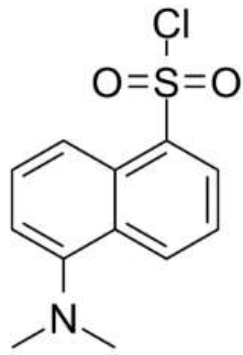

d

Figure 1. Dervatization agents (a:NBD-Cl; b: Fluorescamine;c: NBD-F; d: Dansyl chloride)

REFERENCE

Alkathiri, F.A., Al-Outaibib, and M., Darwish, I.A.(2024). A dual-function chromogenic and fluorogenic benzofurazan probe for plazomicin and its innovative utility for development of two microwell assays with high throughput for analysis of drug substance and pharmaceutical formulations. RSC Adv.,14,27215.

Almalkia, A.H., Alqahtanic, A.S., Algarni, M.A., Bamaga, A.K., Alsulami, F.T., Abduljabbar, M.H., Althobaiti, Y.S., and Ramzy, S. (2024). Sustainable fluorescence derivatization approach for spectrofluorimetric quantification of methylphenidate hydrochloride in pharmaceutical formulation and spiked human plasma. Journal of Molecular Structure, 1299,137326.

Altigani, A.M.N., Elbashir, A.A.,and Aboul-Enein, H.Y. (2018). Optimization and Validation of a Fluorescence Method for the Determination of Primaquine in Pharmaceutical Formulation. Current Analytical Chemistry, 14(1),30-35.

Fukushima, T., Kawai, J., Imai, K., and Toyo'oka, T.(2004).Simultaneous determination of D- and L-serine in rat brain microdialysis sample using a column-switching HPLC with fluorimetric detection. Biomed. Chromatogr., 18, 813–819.

Hamad, A.A., Mahdi, W.A., Alshehri, S., Alsehli, B.R., and El Hamd, M.A.(2025). A new fluorimetric method based on a chemical sensing strategy through the dansylation reaction for the nano-level quantification of cinacalcet hydrochloride, a selective calcimimetic agent. Microchemical Journal, 216, 114655.

Karasakal, A., and Ulu Tatar, S.(2014). Spectrofluorimetric Determination of Nateglinide in Pure and Pharmaceutical Preparations Through Derivatization with 4Chloro7nitrobenzo2oxa1,3diazole. Optics and Spectroscopy,116(1), 52–55.

Karasakal, A., Ulu Tatar, S., and Unal Ozer, D. (2015). Spectrofluorimetric Determination of Famciclovir in Pure and Pharmaceutical Preparations. Optics and Spectroscopy, 119(2),318-321.

Karasakal, A.(2015). Development and Validation of a Sensitive Spectrofluorimetric Method for the Determination of Cilazapril of Human Plasma, Urine, in Pure and Pharmaceutical Preparations. Optics and Spectroscopy, 119 (2),322–326.

Karasakal, A., and Ulu Tatar, S.(2015). Sensitive Spectrofluorimetric Determination of Alfuzosin in Pharmaceutical Preparations and Human Urine Using Dansyl Chloride. Journal of Analytical Chemistry, 70(6),708–711.

Karasakal, A., and Ulu Tatar, S.(2014). Validated spectrofluorimetric method for the determination of tamsulosin in spiked human urine, pure and pharmaceutical preparations. Luminescence, 29,239–242.

Marzouqa, M.A., Salman, B.I., Hussein, S.A., and Ali, M.F.B.(2019). Utility of fluorescamine-based approach for highly sensitive spectrofluorimetric determination of Ceftazidime and Vancomycin in pharmaceuticals and real human plasma.Microchemical Journal, 145, 218-225.

Nassar, M.W., Serag, A., Hasan, M.A.,and Kame, M.(2026). Development of Stability- Indicating Spectrofluorimetric Method for Favipiravir Determination Using 4- Fluoro- 7- Nitrobenzo- 2- Oxa- 1,3- Diazole Derivatization: Application to Quality Control and Therapeutic Drug Monitoring. Luminescence, 41,e70516.

Omar, M.A., Anwer, E.F., and NourEl-Deen, D.A.M.(2021). Derivatization of tranexamicacid for its rapid spectrofluorimetric determination in pure form and pharmaceutical formulations: Application in human plasma. Spectrochimica Acta Part A:Molecular and Biomolecular Spectroscopy, 247,119111.

Omar, M.A., Abdelmageed, O.H., Derayea,S.M., and Attia, T.Z.(2014). Spectrofluorimetric protocol for antidepressant drugs in dosage forms and human plasma through derivatization with dansylchloride.Arabian Journal of Chemistry,10,S3197–S3206.

Onal, C., and Kepekci Tekkeli, S.E.(2020). Spectrofluorimetric analysis Research Article www.jrespharm.com of ticagrelor in pharmaceutical formulations and spiked human plasma using 1-dimethylaminonaphthalene-5-sulphonyl chloride reagent. J Res Pharm., 24(5), 765-773.

Onal, A. (2011). Spectrophotometric and spectrofluorimetric determination of some drugs containing secondary amino group in bulk drug and dosage forms via derivatization with 7-chloro-4-nitrobenzofurazon. Quim. Nova, 34(4), 677-682.

Péreza, A.L., Tibaldo, G., Sánchez, G.H.,Siano, G.G.,Marsili,N.R.,and Schenone, A.V.(2019). A novel fluorimetric method for glyphosate and AMPA determination with NBD-Cl and MCR-ALS. Spectrochimica Acta Part A: Molecular and Biomolecular Spectroscopy. 214, 119–128.

Tekeli, E.S.(2017). Spectrofluorimetric Method for the Determination of Tolterodine In Human Plasma and Pharmaceutical Preparations by Derivatization with Dansyl Chloride. Bezmialem Science, 5, 50-5.

Ulu Tatar, S.T., and Cakar, M.B.(2012). A Sensitive Spectrofluorimetric Method for the Determination of Ranitidine Hydrochloride in Pharmaceutical Preparation. Optics and Spectroscopy, 113, (2), 126–130

Ulu Tatar, S.(2011). New and Sensitive Spectrofluorimetric Method for the Determination of Non-Steroidal Anti inflammatory Drugs, Etodolac and Diclofenac Sodium in Pharmaceutical Preparations through Derivatization with 7-fluoro-4-nitrobenzo-2-oxa-1,3-diazole. Journal of Food and Drug Analysis, 19,(1), 94-101.

Walash, M.I., El-Enany, N., and Askar, H. (2015). Validated spectrofluorimetric method for the determination of carbamazepine in pharmaceutical dosage forms after reaction with 4-chloro-7-nitrobenzo-2-oxa-1,3-diazole (NBD-Cl).Luminescence, 30, 1119–1124.

Taxicab Circular Inverses of Taxicab Circles: An Analytic Classification

Ayşe BAYAR[1]

Seyit Ali AYDIN[2]

1- Prof. Dr.; Department of Mathematics and Computer Science, Eskişehir Osmangazi University, Türkiye. akorkmaz@ogu.edu.tr ORCID No: 0000-0002-2210-5423

2- Mathematics Teacher, Beyhan-Rıfat Çıkıllıoğlu Anadolu High School, Türkiye. seyitaliaydin@mail.com ORCID No: 0000-0002-9502-6152

ABSTRACT

This chapter develops a complete analytic description of the images of taxicab circles under the taxicab circular inversion $I_T(O,r)$ determined by $C_T(O,r)$. Starting with a source circle of arbitrary center and radius, we derive a global implicit equation and then resolve it edge by edge and quadrant by quadrant. This decomposition proves that every source-edge subsegment contained in a fixed quadrant is mapped either to a bounded line segment or to a parabolic arc. A crucial distinction is made between a supporting line that passes through the inversion center and a finite edge segment that actually contains the center: the former may still have a bounded image, whereas rays occur only in the latter situation. The inverse curves are classified according to the position of the source center relative to the coordinate axes and separator lines and according to four critical parameters. For a center $M = (a,b)$ with $a > b > 0$, $\delta_1 = b$ and $\delta_1 = b$ mark the axis-contact thresholds, $D = a + b$ marks passage through the inversion center, and $\Delta = \mathrm{a} - \mathrm{b}$ identifies the algebraic degeneration of one parabolic component into a finite segment. Concentric circles remain taxicab circles, while nonconcentric circles become piecewise-quadratic curves assembled from line segments, parabolic arcs, and, in the unbounded case, exactly two rays. Self-contained proofs, equality cases, a complete classification table, worked examples, and figures verified by direct pointwise inversion are included.

Keywords – taxicab metric; taxicab circle; circular inversion; parabolic arc; line segment; non-Euclidean geometry

1. INTRODUCTION

Circular inversion is one of the classical transformations of plane geometry. Its origins are commonly traced to the geometric investigations of Apollonius, while its systematic development is associated with the work of Steiner in the nineteenth century. For a fixed Euclidean circle with center O and radius r, each point P≠O is mapped to the unique point P′ on the ray OP satisfying $OP \cdot OP' = r^2$. In the Euclidean plane, this transformation preserves generalized circles: a line not passing through the inversion center is mapped to a circle through that center; a circle through the center is mapped to a line not passing through it; and a circle avoiding the center is mapped to another circle. These familiar properties are closely tied to the Euclidean norm of the displacement vector and therefore change substantially when the underlying distance is replaced by a non-Euclidean metric (Blair, 2000; Nickel, 1995).

The taxicab plane is the Cartesian plane equipped with the metric induced by the ℓ_1 norm of displacement vectors. Although its points and ordinary straight lines coincide with those of the Euclidean analytic plane, the distance between two points is measured by the sum of the absolute horizontal and

vertical displacements. Krause (1975) gave the first systematic account of taxicab geometry, and Schattschneider (1984) subsequently described its isometry group. Later studies broadened the analytic foundations of the subject through taxicab trigonometry (Akça & Kaya, 1997), distance formulae in three-dimensional taxicab space (Akça & Kaya, 2004a), norms in higher-dimensional taxicab spaces (Akça & Kaya, 2004b), and Voronoi structures in the taxicab plane (Akça & Çalış, 2021). In this geometry, a taxicab circle is not a Euclidean circle but a square whose diagonals are parallel to the coordinate axes. Consequently, taxicab circular inversion remains a radial transformation, but it is not conformal in the Euclidean sense.

The first systematic treatment of circular inversion in the taxicab plane was given by Bayar and Ekmekçi (2014), who established the basic pointwise and metric properties of the transformation. During the same period, inversion was also extended to other metric settings. Ramirez et al. (2015) introduced p-circle inversion, thereby placing Euclidean and taxicab inversions within a common p-norm perspective. Subsequent studies considered circular inversion in the maximum plane (Yüca & Can, 2020), maximum spherical inversion (Cırık & Ekmekçi, 2022), and the maximum circular inverses of lines and circles (Ekmekçi, 2023a, 2023b). These contributions are cited only to situate the present chapter within the wider literature on non-Euclidean metric inversion; all arguments developed below are carried out entirely in the taxicab plane.

Within the taxicab setting, Aydın (2023) examined the inverses of lines and taxicab circles and organized the resulting curves according to the regions determined by the coordinate axes and the sides of the inversion circle. Bayar and Aydın (2024) later presented a systematic analytic study of line inverses. They showed that a line not passing through the inversion center generally becomes a closed curve formed by parabolic arcs, whereas a line parallel to a side of the taxicab inversion circle produces an image containing both a parabolic arc and a finite line segment. These results reveal that, unlike Euclidean circular inversion, taxicab circular inversion naturally produces piecewise quadratic curves whose components depend on the position of the source object relative to the coordinate regions.

The purpose of this chapter is to derive the inverse images of taxicab circles directly from the coordinate formula for $I_T(O,r)$ and to provide a complete classification that includes all limiting and exceptional cases. We first obtain a global equation involving absolute values and then decompose it with respect to the four sides of the source taxicab circle and the four coordinate regions of the image plane. This decomposition identifies precisely when the inverse image contains finite line segments, parabolic arcs, or rays. In addition to the thresholds at which the source circle meets or crosses the coordinate axes, the algebraic value $\Delta = a - b$—corresponding to the passage of a supporting line through the inversion center—is treated explicitly.

The regional observations and circle configurations presented in Aydın's master's thesis provide an important starting point for the present analysis and are cited accordingly (Aydın, 2023). The treatment developed here reorganizes and extends that material through a unified edge equation, a corrected threshold classification, independent proofs, analytic examples, and newly prepared figures. In this way, the chapter offers a coherent framework for understanding how the position of the center and the radius of a source taxicab circle determine the geometry and topology of its inverse image.

2. PRELIMINARIES

2.1. The taxicab metric and taxicab circles

Definition 2.1. Let $\mathbb{R}^2$ contain the points $P = (x_1, y_1)$ and $Q = (x_2, y_2)$. Their taxicab distance is

$$d_T(P, Q) = |x_1 - x_2| + |y_1 - y_2|.$$

For a vector $v = (x, y) \in \mathbb{R}^2$, the taxicab norm is

$$\| (x, y) \|_T = |x| + |y|.$$

Accordingly, $d_T(P, Q)$ is the taxicab norm of the displacement vector from P to Q. The plane $\mathbb{R}^2$ equipped with this metric is denoted by $\mathbb{R}^2_T$. In particular, the norm is assigned to a vector, whereas the distance $d_T(P, Q)$ is assigned to the ordered pair of points *P* and *Q*.

Definition 2.2. A taxicab circle with center $M = (a, b)$ and radius $\rho > 0$ is the set

$$C_T(M, \rho) = \{(x, y) \in \mathbb{R}^2 : |x - a| + |y - b| = \rho\}.$$

Its vertices are $(a + \rho, b)$, $(a, b + \rho)$, $(a - \rho, b)$ and $(a, b - \rho)$. Thus it is a Euclidean square whose sides have slopes $+1$ and -1. Its sides may be represented by

$$\varepsilon_1(x - a) + \varepsilon_2(y - b) = \rho, \qquad \varepsilon_1, \varepsilon_2 \in \{-1, 1\},$$

where the appropriate inequalities select the finite side rather than the entire supporting line. These standard facts provide the geometric basis for the piecewise analysis of inverse curves (Aydın, 2023).

The coordinate axes divide the plane into four closed quadrants. Within each open quadrant, the taxicab norm of the vector $v = (x, y)$ is represented by a linear expression. More precisely, if $\sigma_1 = sgn(x)$ and $\sigma_2 = sgn(y)$, then

$$|x| + |y| = \sigma_1 x + \sigma_2 y.$$

This quadrantwise linearity of the taxicab norm is the algebraic source of the piecewise-quadratic character of taxicab inversion.

2.2. Taxicab circular inversion

Definition 2.3. Choose a taxicab circle centered at *O* with radius $r > 0$ as the inversion circle:

$$\mathcal{C} = C_T(O, r) = \{(x, y) : |x| + |y| = r\}, \qquad r > 0,$$

Let this circle be fixed. For $P \neq O$, its taxicab inverse $P' = I_{T(O,r)}(P)$ is the unique point on the ray OP satisfying

$$d_T(O,P)d_T(O,P') = r^2.$$

This condition determines a unique point. If $P = (x, y)$ and $s = |x| + |y|$, then P' is obtained from P by multiplication by the positive scalar r^2/s^2. Hence

$$I_{T(O,r)}(x,y) = \left(\frac{r^2 x}{(|x| + |y|)^2}, \frac{r^2 y}{(|x| + |y|)^2}\right).$$

If the inversion circle is centered at $O_0 = (h, k)$, translation gives

$$I_{T(O_0,r)}(x,y) = O_0 + \frac{r^2}{(|x-h| + |y-k|)^2}(x-h, y-k).$$

Translations are taxicab isometries; therefore, placing the inversion center at $O = (0,0)$ causes no loss of generality. Unless otherwise stated, this convention will be used throughout. For a subset A of the taxicab plane that does not contain *O*, its inverse image is written $I_{T(O,r)}(A) = \{I_{T(O,r)}(P): P \in A\}$.

Proposition 2.1. The taxicab circular inversion $I_{T(O,r)}$ has the following properties.

(i) It is involutive: for every $P \neq O$, one has $I_{T(O,r)}\left(I_{T(O,r)}(P)\right) = P$.

(ii) Every point of the inversion circle $\mathcal{C}$ is fixed.

(iii) Points inside $\mathcal{C}$ are mapped outside $\mathcal{C}$, and points outside are mapped inside.

(iv) Every ray issuing from O is invariant as a set.

Proof. Let $s = d_T(O,P)$. Since $I_{T(O,r)}(P) = P'$ lies on the radial direction from O through P and is obtained with the multiplier r^2/s^2, we have $d_T(O,P') = \frac{r^2}{s^2}$. Applying the transformation a second time gives

$$I_{T(O,r)}\left(I_{T(O,r)}(P)\right) = \frac{r^2}{(r^2/s)^2}\frac{r^2}{s^2}P = P.$$

The remaining assertions follow at once from

$$d_T\left(O, I_{T(O,r)}(P)\right) = \frac{r^2}{d_T(O,P)}$$

and from the positivity of the radial multiplier. □

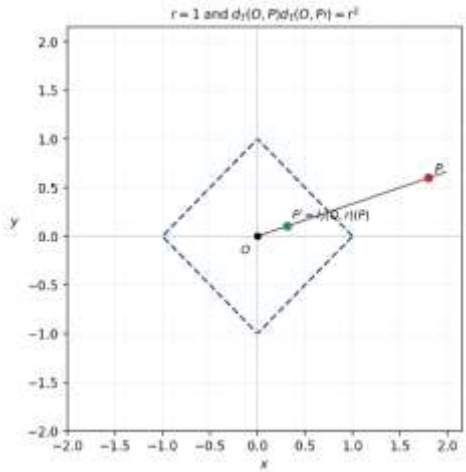

Figure 1: A point and its taxicab circular inverse on the same ray.

2.3. The extended taxicab plane

The origin has no finite inverse, and no finite point is mapped to the origin. As in classical inversion theory, one may adjoin a single point at infinity and define

$$I_{T(O,r)}(O) = \infty, \qquad I_{T(O,r)}(\infty) = O.$$

With this convention, $I_T(O,r)$ becomes a bijection of the extended taxicab plane $\widehat{\mathbb{R}}_T^2 = \mathbb{R}_T^2 \cup \{\infty\}$. The extension is particularly useful when the source curve passes through O. In the ordinary taxicab plane, the image is then open and unbounded; in the extended plane, its unbounded branches meet at ∞.

3. ANALYTIC EQUATION OF THE INVERSE OF A TAXICAB CIRCLE

Let the source circle be

$$C_T(M,\rho): |x-a| + |y-b| = \rho,$$

and let $\Gamma = I_{T(O,r)}\big(C_T(M,\rho)\big)$ be its inverse with respect to $C_T(O,r)$. Write an image point as $Q = (X,Y)$ and set

$$s = |X| + |Y|.$$

Since the inversion is involutive, the corresponding source point is

$$(x,y) = I_{T(O,r)}(X,Y) = \left(\frac{r^2X}{s^2}, \frac{r^2Y}{s^2}\right).$$

Substitution into the source-circle equation yields the following global implicit relation.

Theorem 3.1. The inverse curve Γ consists precisely of the nonzero points (X,Y) satisfying

$$|r^2X - as^2| + |r^2Y - bs^2| = \rho s^2, \qquad s = |X| + |Y|.$$

Proof. In the equation $|x-a| + |y-b| = \rho$, substitute $x = r^2X/s^2$ and $y = r^2Y/s^2$, and multiply both sides by $s^2 > 0$.□

Although this equation is compact, its geometry becomes transparent only after it is restricted simultaneously to one side of the source circle and one quadrant of the image plane.

3.1. Edgewise equations

$\varepsilon = (\varepsilon_1, \varepsilon_2) \in \{-1,1\}^2$ be fixed. A supporting line of one side of the taxicab circle is

$$\varepsilon_1(x-a) + \varepsilon_2(y-b) = \rho.$$

Equivalently, it may be written as

$$\varepsilon_1 x + \varepsilon_2 y = c_\varepsilon, \qquad c_\varepsilon = \rho + \varepsilon_1 a + \varepsilon_2 b.$$

After inversion, the supporting-line equation becomes

$$\boxed{r^2(\varepsilon_1 X + \varepsilon_2 Y) = c_\varepsilon(|X| + |Y|)^2.}$$

In the quadrant indexed by $\sigma = (\sigma_1, \sigma_2)$, where $\sigma_i = sgn(X_i)$, for i=1,2, this equation reduces to

$$r^2(\varepsilon_1 X + \varepsilon_2 Y) = c_\varepsilon(\sigma_1 X + \sigma_2 Y)^2.$$

The linear form on the left and the linear form inside the square are either proportional or linearly independent. This alternative determines the type of the image piece.

Proposition 3.2. Let E be a closed subsegment of a taxicab-circle edge obtained after cutting the edge by the coordinate axes, and suppose E lies in one fixed quadrant. Then $I_{T(O,r)}$(E) has exactly one of the following forms.

(i) If $c_\varepsilon \neq 0$ and the vector $(\varepsilon_1, \varepsilon_2)$ is proportional to (σ_1, σ_2), then $I_{T(O,r)}$(E) is a finite line segment parallel to a side of the inversion circle.

(ii) If $c_\varepsilon \neq 0$ and $(\varepsilon_1, \varepsilon_2)$ is not proportional to (σ_1, σ_2), then $I_{T(O,r)}$(E) is a parabolic arc.

(iii) If $c_\varepsilon = 0$, the supporting line passes through the inversion center and the inverse remains on that same line. If $O \notin E$, the image is a finite line segment; if O is an endpoint of E, the image is one ray; and if O is an interior point of E, the image consists of two oppositely directed rays.

Proof. In the proportional case, $\varepsilon_1 X + \varepsilon_2 Y = \lambda(\sigma_1 X + \sigma_2 Y)$, so away from O the image equation reduces to a linear relation of the form $\sigma_1 X + \sigma_2 Y = constant$. If E is compact and disjoint from O, $I_{T(O,r)}$(E) is therefore a finite line segment. In the independent case, take $p = \sigma_1 X + \sigma_2 Y$ and $q = \varepsilon_1 X + \varepsilon_2 Y$ as affine coordinates. The equation becomes $q = (c_\varepsilon / r^2)p^2$, and the image is a parabolic arc. If $c_\varepsilon = 0$, the image equation is $\varepsilon_1 X + \varepsilon_2 Y = 0$, so the supporting line is invariant under radial inversion. Unboundedness, however, is caused not by the supporting line alone but by the presence of O in the finite source segment. If $O \notin E$, then $d_T(O, E) > 0$ and the image is bounded. If O is an endpoint of E, $E \setminus \{O\}$ has one connected component; if O is an interior point, it has two. Their inverse images are, respectively, one ray or two rays. □

Figure 2 shows how the four sides of a taxicab circle are divided into the analytic pieces that form its inverse.

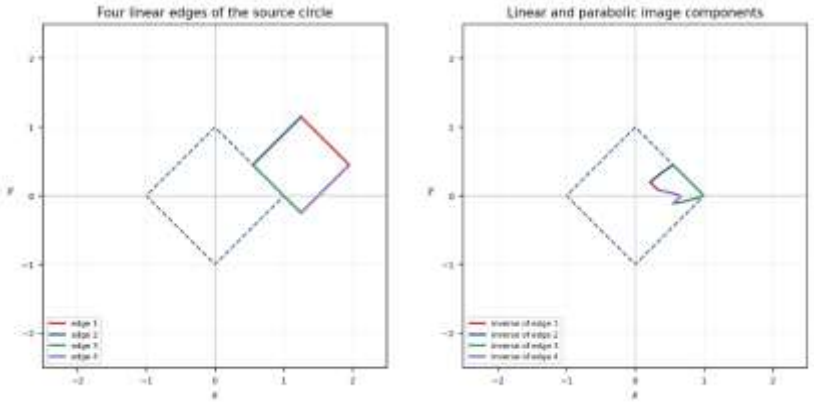

Figure 2: Edgewise decomposition of a taxicab circle and the corresponding linear and parabolic image pieces.

3.2. Closed and open inverse curves

Theorem 3.3. Let $M = (a, b)$, $D = d_T(O, M) = |a| + |b|$, and $\rho > 0$.

(i) If $\rho \neq D$, the inverse of $C_T(M, \rho)$ is a closed and bounded curve in the ordinary taxicab plane.

(ii) If $\rho = D$, the source circle passes through O. Its inverse is an open, unbounded curve composed of finite line segments, parabolic arcs, and exactly two rays. In the extended taxicab plane, the two rays meet at ∞.

Proof. The inversion center O lies on the source taxicab circle $C_T(M, \rho)$ if and only if the taxicab distance from O to the center $M = (a, b)$ is equal to the radius ρ. Equivalently, $O \in C_T(M, \rho) \Leftrightarrow |a| + |b| = \rho$. If $\rho \neq D$, the compact source circle has positive taxicab distance from O; inversion is continuous on that compact set, so its image is compact, hence closed and bounded. If $\rho = D$, the circle has two local branches at O. When O is a vertex, the two incident edge pieces are separated there; when O lies in the interior of an edge, the edge is split into two components by O. Proposition 3.2(iii) maps those two components to two rays. All remaining pieces stay away from O and therefore become finite line segments or parabolic arcs. □

4. CLASSIFICATION OF THE INVERSES OF TAXICAB CIRCLES

The isometries of the taxicab plane include translations, reflections in the coordinate axes and separator lines, and rotations through integer multiples of π/2. Hence the center may be moved to a convenient representative position without changing either the number or the type of image components. The following classification is obtained directly from the edgewise equations in Proposition 3.2.

4.1. Concentric taxicab circles

Theorem 4.1. If the source circle is concentric with the inversion circle, then

$$I_{T(O,r)}\big(C_T(O,\rho)\big) = C_T\left(O, \frac{r^2}{\rho}\right).$$

Thus the stated image is obtained. In particular, the inversion circle $C_T(O,r)$ is fixed pointwise.

Proof. For every $P \in C_T(O,\rho)$, one has $d_T(O,P) = \rho$. Therefore

$$d_T\left(O, I_{T(O,r)}(P)\right) = \frac{r^2}{p}.$$

Conversely, involutivity shows that every point of the target circle arises in this way. □

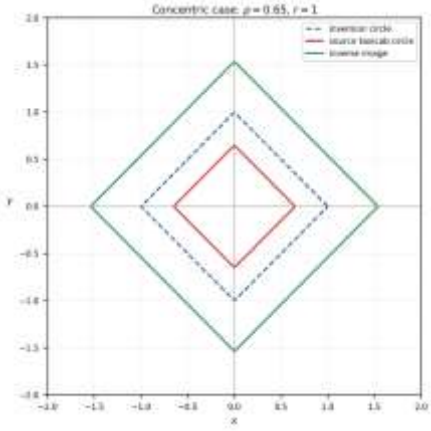

Figure 3: A concentric taxicab circle and its concentric inverse.

4.2. Taxicab circles with center on a coordinate axis

After a suitable taxicab isometry, assume $M = (a, 0)$ with $a > 0$. Then $D = d_T(O,M) = a$.

Theorem 4.2. Let $I_T(O,r)$ denote the taxicab circular inversion with respect to the taxicab circle C_T(O,r), where O=(0,0) and r>0. Let $C_T(M,\rho)$ be the taxicab circle

$$C_T(M,\rho) = \{(x,y) \in \mathbb{R}^2 : |x-a| + |y| = \rho\}$$

with center M=(a,0), where a>0 and ρ>0. Then the inverse image $I_{T(O,r)}(C_T(M,\rho))$ is classified as follows:

(i) If 0<ρ<a, the inverse image is a four-piece closed and bounded curve consisting of two finite line segments and two parabolic arcs.

(ii) If ρ=a, the inverse image is a four-piece open and unbounded curve consisting of two finite line segments and two rays.

(iii) If ρ>a, the inverse image is a six-piece closed and bounded curve consisting of four finite line segments and two parabolic arcs.

Proof. The four supporting lines of $C_T(M,\rho)$ have equations $x-a\pm y=\pm\rho$. If $0<\rho<a$, the source circle lies in the half-plane $x>0$, and Proposition 3.2 gives two line segments and two parabolic arcs. At $\rho=a$, the left vertex coincides with O. The two incident edges are mapped to the rays $\{(t,t): t\geq r^2/(4a)\}$ and $\{(t,-t): t\geq r^2/(4a)\}$ on $y=x$ and $y=-x$. Thus the rays begin at finite points, not at O. The remaining two edges become finite line segments. If $\rho>a$, the source circle crosses the y-axis; two edges are divided at their axis-intersection points, producing four line segments and two parabolic arcs in total. □

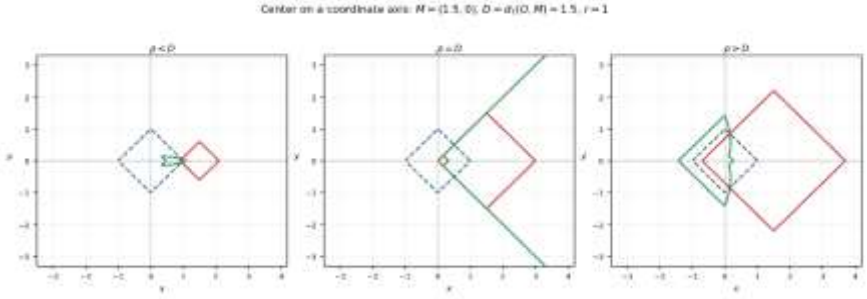

Figure 4: Inverses of taxicab circles whose centers lie on a coordinate axis.

4.3. Taxicab circles with center on a separator line

Assume $M=(a,a)$ with $a>0$. The center lies on the separator line $y=x$. Set

$$\delta=a, \qquad D=2a.$$

Here $\delta=a$ is the taxicab distance from M to either coordinate axis, whereas $D=d_T(O,M)=2a$ is the distance from the center to the inversion center.

Theorem 4.3. Let $I_T(O,r)$ denote the taxicab circular inversion with respect to the taxicab circle C_T(O,r), where $O=(0,0)$ and $r>0$. Let

$$C_T(M,\rho)=\{(x,y)\in\mathbb{R}^2: |x-a|+|y-a|=\rho\}$$

be a taxicab circle with center $M=(a,a)$, where $a>0$ and $\rho>0$. Define $\delta=a,\ D=2a$. Then the inverse image $I_T(O,r)(C_T(M,\rho))$ is classified as follows:

(i) If $0<\rho\leq\delta$, the inverse is a four-piece closed curve, symmetric about $y=x$, consisting of two line segments and two parabolic arcs.

(ii) If $\rho>\delta$ and $\rho\neq D$, the inverse is an eight-piece closed curve consisting of four line segments and four parabolic arcs.

(iii) If $\rho=D$, the inverse is a seven-piece open curve consisting of three finite line segments, two parabolic arcs, and two rays.

Proof. The vertices of $C_T((a,a),\rho)$ are $(a \pm \rho, a)$ and $(a, a \pm \rho)$. For $0 < \rho \leq a$, the circle remains in the closure of the first quadrant. The equality ρ=a is the tangency case and does not change the number of analytic pieces. Proposition 3.2 yields two line segments and two parabolic arcs. When ρ>a, the source circle crosses both coordinate axes; except at $\rho = 2a$, the inverse has four line segments and four parabolic arcs. At $\rho = 2a$, the edge $x + y = 0$ contains O in its interior. Its two components are mapped to the rays $\{(-t,t): t \geq r^2/(4a)\}$ and $\{(t,-t): t \geq r^2/(4a)\}$. Their finite initial points leave an open interval containing O between the rays. The remaining pieces form three finite line segments and two parabolic arcs. □

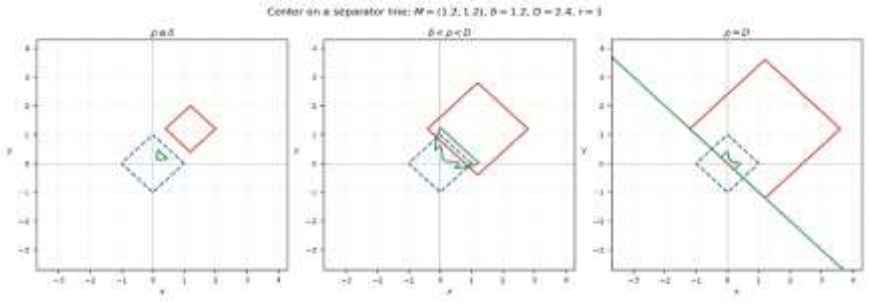

Figure 5: Inverses of taxicab circles whose centers lie on a separator line.

4.4. Taxicab circles with centers in general position

By combining reflections with an interchange of coordinates, any center that lies on neither a coordinate axis nor a separator line may be represented in the form

$$M = (a,b), \qquad a > b > 0.$$

Define the following quantities:

$$\delta_1 = b, \quad \delta_2 = a, \quad \Delta = a - b, \quad D = a + b.$$

The values δ_1 and δ_2 are the taxicab distances from M to the two coordinate axes, and D is the distance from M to the inversion center. The value Δ is an algebraic threshold at which the supporting line of one source edge passes through O. When $\rho = \Delta$, the relevant edge does not contain O, so its inverse is a finite segment on $y = x$.

Theorem 4.4. Let $I_T(O,r)$ denote the taxicab circular inversion with respect to the taxicab circle C_T(O,r), where $O = (0,0)$ and $r > 0$. Let C_T(M,ρ) be a taxicab circle with center $M = (a,b)$, where $a > b > 0$ and $\rho > 0$. Define $\delta_1 = b$, $\delta_2 = a$, $\Delta = a - b$, and $D = a + b$.

(i) If $0 < \rho \leq \delta_1$ and $\rho \neq \Delta$, the inverse is a four-piece closed curve consisting of two line segments and two parabolic arcs.

(ii) If $\delta_1 < \rho \leq \delta_2$ and $\rho \neq \Delta$, the inverse is a six-piece closed curve consisting of three line segments and three parabolic arcs.

(iii) If $\rho > \delta_2$ and $\rho \neq D$, the inverse is an eight-piece closed curve consisting of four line segments and four parabolic arcs.

(iv) If $\rho = D$, the inverse is a seven-piece open curve consisting of three finite line segments, two parabolic arcs, and two rays.

(v) If $\rho = \Delta$, two subcases arise. When $\Delta \leq \delta_1$, the inverse is a four-piece closed curve made of three line segments and one parabolic arc. When $\delta_1 < \Delta < \delta_2$, the inverse is a six-piece closed curve made of four line segments and two parabolic arcs.

Proof. The vertices of $C_T((a, b), \rho)$ are $(a \pm \rho, b)$ and $(a, b \pm \rho)$. If $0 < \rho \leq b$, $\rho \neq \Delta$ the generic image has four analytic components—even at $\rho = b$, where one vertex touches the x−axis—and Proposition 3.2 gives two line segments and two parabolic arcs. If $b < \rho \leq a$, $\rho \neq \Delta$ the circle crosses the x-axis but not the y-axis; two edges are cut by the axis, giving three line segments and three parabolic arcs. If $\rho > a$, both coordinate axes are crossed, and for $\rho \neq D$ the inverse has four line segments and four parabolic arcs. At $\rho = D = a + b$, the edge $x + y = 0$ contains O in its interior. Its two components are mapped to $\left\{(-t, t): t \geq \frac{r^2}{4b}\right\}$ and $\left\{(t, -t): t \geq \frac{r^2}{4a}\right\}$, while the remaining pieces give three finite line segments and two parabolic arcs. Finally, if $\rho = \Delta = a - b$, the source edge on the supporting line $y = x$ is the finite segment joining (b, b) and (a, a), and it does not contain O. Its inverse is the finite segment on $y = x$ joining $(r^2/(4a), r^2/(4a))$ and $(r^2/(4b), r^2/(4b))$. Hence, when $\Delta \leq b$, one parabolic arc in the generic four-piece case degenerates into a line segment, yielding three line segments and one parabolic arc. When $\Delta > b$, the same degeneration occurs in the generic six-piece case, yielding four line segments and two parabolic arcs. At $\rho = \delta_1$ or $\rho = \delta_2$, zero-length components are not counted separately; adjacent pieces meet at their common endpoint. □

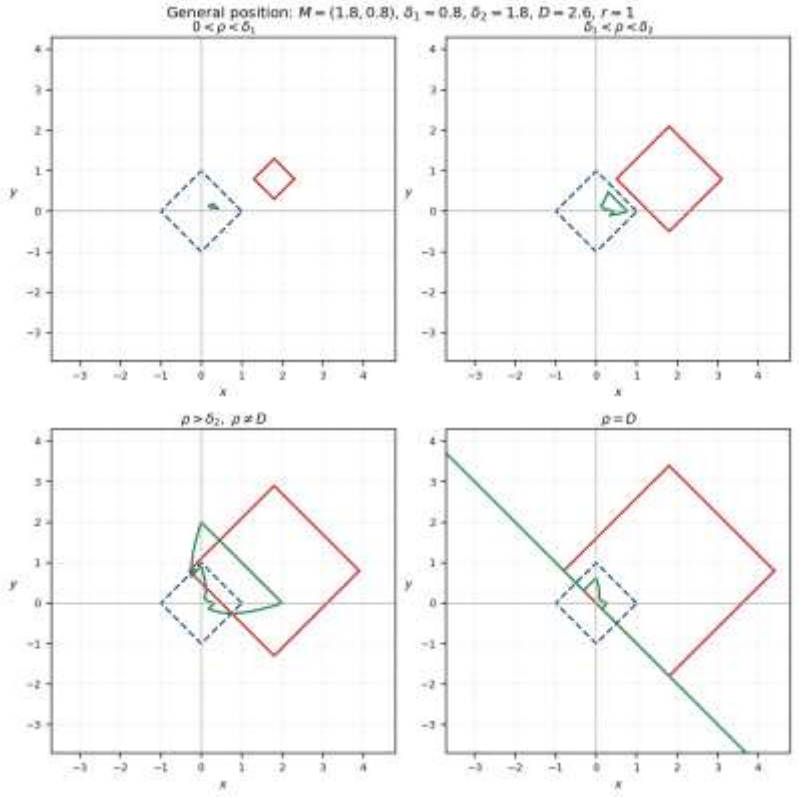

Figure 6: Inverse images of a taxicab circle with center in general position.

The preceding theorems, together with the special-threshold analysis, cover every boundary case. Concentric circles remain taxicab circles. For a center on a coordinate axis, the image changes from a closed curve to an open two-ray curve at $\rho = D$. For a center on a separator line, the closed images have four or eight analytic pieces, while $\rho = D$ gives a seven-piece open curve. In general position, δ_1 and δ_2 govern the axis crossings, D governs the topological opening, and Δ marks the algebraic conversion of one parabolic piece into a finite line segment.

4.5. Complete classification and special thresholds

Table 1 summarizes the generic, boundary, and exceptional cases of Theorem 4.4. In the table, "segment" means a finite line segment, "parabolic arc" denotes a bounded parabolic component, and "ray" denotes an unbounded linear component. The threshold Δ does not open the curve; it only converts one parabolic component into a finite segment on the same supporting line.

Table 1: Complete classification of taxicab-circle inverses for a center in general position.

Condition	Line segments	Parabolic arcs	Rays	Curve type
$0 < \rho \le \delta_1, \rho \ne \Delta$	2	2	0	Closed
$\delta^1 < \rho \le \delta^2, \rho \ne \Delta$	3	3	0	Closed
$\rho > \delta_2, \rho \ne D$	4	4	0	Closed
$\rho = D$	3	2	2	Open
$\rho = \Delta \le \delta_1$	3	1	0	Closed
$\delta_1 < \rho = \Delta < \delta_2$	4	2	0	Closed

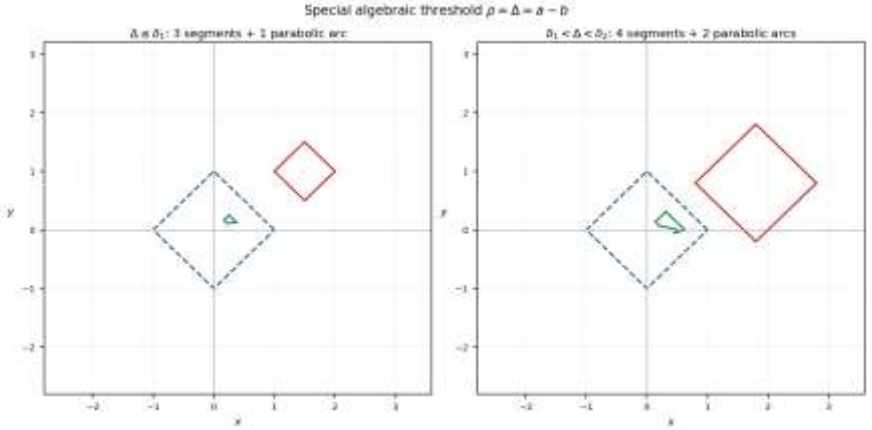

Figure 7: The two boundary classes that occur at the algebraic threshold $\rho = \Delta = a - b$.

5. ILLUSTRATIVE ANALYTIC EXAMPLES

Example 5.1. A small circle contained in one active quadrant

Consider inversion in the unit taxicab circle and the following source circle:

$$|x - 3/2| + |y - 1/2| = 1/2.$$

Here $M = (3/2,1/2)$, $\delta_1 = 1/2$, $\delta_2 = 3/2$ and $D = 2$; hence the radius is exactly the first transition value. The global inverse equation is

$$\left|X - \frac{3}{2}S^2\right| + \left|Y - \frac{1}{2}S^2\right| = \frac{1}{2}S^2, \qquad S = |X| + |Y|.$$

In this equation, the side $x + y = 5/2$ has $\varepsilon = (1,1)$ and $c_\varepsilon = 5/2$. In the first quadrant, where $S = X + Y$, the inverse equation becomes

$$X + Y = \frac{2}{5}.$$

This is a line segment parallel to one side of the inversion circle. For the side $x - y = 3/2$, one obtains

$$X - Y = \frac{3}{2}(X + Y)^2.$$

This is a parabola in the first quadrant. The remaining components are obtained by using the appropriate quadrant signs and by restricting each equation to the inverse of the corresponding finite source edge.

Example 5.2. A circle centered on the positive x-axis

Consider the circle $|x - 1| + |y| = \frac{1}{2}$, $\rho = 1/2 < D = 1$. Since the displayed inequality holds, Theorem 4.2 shows that the inverse is a four-piece closed curve with two line segments and two parabolic arcs. Its global equation is

$$|X - S^2| + |Y| = \frac{1}{2}S^2.$$

The source circle is separated from *O*; hence its inverse is compact. The two edges whose supporting directions are proportional to the local linear expression for $S = |X| + |Y|$ generate finite line segments, whereas the remaining two edges generate parabolic arcs.

If the radius is changed to $\rho = 1$, the source circle passes through the origin. The two half-edges incident with O are mapped to two rays, while the remaining edges produce two bounded line segments. This is the four-piece open case.

Example 5.3. A circle centered on a separator line

Consider $M = (1,1)$, $\rho = \frac{3}{2}, r = 1$. Here $\delta = 1 < \rho < 2 = D$. Theorem 4.3 gives an eight-piece closed image with four line segments and four parabolic arcs. The curve is symmetric about the separator line $y = x$. Its global equation is

$$|X - S^2| + |Y - S^2| = \frac{3}{2}S^2.$$

Although the source circle intersects both coordinate axes, it does not pass through the origin. Its inverse therefore remains bounded. This example illustrates how crossing quadrant boundaries increases the number of analytic components without changing the topology of the image.

Example 5.4. A six-piece inverse in general position

Consider $M = \left(\frac{9}{5}, \frac{4}{5}\right)$, $\rho = \frac{6}{5}$, $r = 1$.

In this case

$$\delta_1 = \frac{4}{5} < \rho = \frac{6}{5} < \delta_2 = \frac{9}{5}.$$

Theorem 4.4 shows that the inverse consists of three line segments and three parabolic arcs. One vertex of the source circle has crossed the nearer coordinate axis, while the circle has not yet reached the farther axis. Two source edges are therefore split into additional quadrant pieces, whereas the remaining edges continue to contribute a single analytic component. The

example makes clear how the component count reflects the number of coordinate-axis boundaries crossed by the source circle.

Example 5.5. The algebraic threshold ρ=Δ

Let $M = (\frac{9}{5}, \frac{4}{5})$, $\rho = 1$, and $r = 1$. Then $\delta_1 = \frac{4}{5}$, $\delta_2 = \frac{9}{5}$, $\Delta = 1$, and $D = \frac{13}{5}$, so $\delta_1 < \rho = \Delta < \delta_2$. The source edge lying on $y = x$ is the finite segment from $(\frac{4}{5}, \frac{4}{5})$ to $(\frac{9}{5}, \frac{9}{5})$, and it does not contain *O*. Its inverse is the finite segment on $y = x$ joining $(\frac{5}{36}, \frac{5}{36})$ to $(\frac{5}{16}, \frac{5}{16})$. By Theorem 4.4(v), the complete inverse is a six-piece closed curve consisting of four line segments and two parabolic arcs. This example demonstrates that a supporting line through *O* does not, by itself, force an unbounded image.

6. RESULTS AND DISCUSSION

The analysis provides a single framework for inverse curves that would otherwise require many separate coordinate cases. Its main consequences may be summarized as follows.

First, the inverse of a general taxicab circle is governed by one global equation:

$$|r^2X - aS^2| + |r^2Y - bS^2| = \rho S^2, \qquad S = |X| + |Y|.$$

The equation is nevertheless intrinsically piecewise, because each absolute-value expression changes its linear form across a coordinate axis. A source edge is divided into one or more subsegments according to its intersections with the axes. In a fixed quadrant, the inverse equation is either linear or quadratic of parabolic type. The coexistence of straight and curved pieces is therefore a direct algebraic consequence of the quadrantwise linear structure of the ℓ_1 norm.

Second, the component classification follows from the local linear algebra of the norm on vectors. Within a fixed quadrant, both the expression for the taxicab norm of $v = (X, Y)$ and the supporting equation of a source edge are linear. If the two forms are proportional, the image component is linear; if they are independent, the image component is parabolic. When a supporting line passes through *O*, the image remains on that line, but rays occur only if the finite source segment itself contains *O*. If the segment is disjoint from *O*, its inverse remains finite. Thus the distinction among a line segment, a parabolic arc, and a ray depends not only on the supporting line but also on the set-theoretic relation between the source segment and *O*.

Third, the critical radii play two different geometric roles. For $M = (a, b)$ with $a > b > 0$, $\delta_1 = b$ and $\delta_2 = a$ are the axis-contact and axis-crossing thresholds. The value $D = a + b$ is the topological threshold at which the source circle passes through the inversion center and the image becomes unbounded. By contrast, $\Delta = a - b$ is an algebraic threshold: at $\rho = \Delta$, one supporting line passes through O, yet the relevant finite edge does not. Consequently, the curve remains closed and only one parabolic component degenerates into a finite line segment. The change of component type and the change of topology are therefore independent phenomena.

Fourth, concentric circles form the only structurally stable family of taxicab circles that is mapped to taxicab circles. Their radii transform according to $\rho \to \frac{r^2}{\rho}$. A nonconcentric source circle generally loses the taxicab-circle shape and becomes a piecewise-quadratic curve. This differs sharply from Euclidean inversion, where a nonconcentric circle that avoids the inversion center remains a circle.

The classification also sharpens the region-based description in Aydın's thesis. Recording whether a circle occupies one, two, three, or four coordinate regions is geometrically informative, but the distance thresholds δ_1, δ_2, and D, together with the algebraic threshold Δ, provide more invariant and computationally useful criteria. They are obtained directly from the center and radius and can be implemented symbolically or numerically (Aydın, 2023).

From a computational standpoint, the edgewise formulation is more reliable than plotting the global absolute-value equation without decomposition. Each source edge can be parameterized separately, the coordinate formula for $I_T(O, r)$ can be applied pointwise, and the resulting parametric image can be checked against the quadrantwise implicit equations. The figures in this chapter were regenerated by comparing these two approaches. In particular, the finite initial points and central gap between the two rays are displayed for $\rho = D$, while the finite linear component is shown explicitly for $\rho = \Delta$.

$$r^2(\varepsilon_1 X + \varepsilon_2 Y) = (\rho + \varepsilon_1 a + \varepsilon_2 b)(\sigma_1 X + \sigma_2 Y)^2$$

produces the exact conic component in each quadrant. It also makes it possible to compute vertices, junction points, tangent directions, and asymptotic rays explicitly.

Finally, the boundary values $\rho = \delta_1$ and $\rho = \delta_2$ are included in the classification. If $\rho = \delta_1$ and $\delta_1 \neq \Delta$, the image has two line segments and two parabolic arcs; if $\rho = \delta_2$, it has three line segments and three parabolic arcs. When $\delta_1 = \Delta$, equivalently $a = 2b$, the special boundary class applies and the image has three line segments and one parabolic arc. Zero-length artificial components are not counted; only maximal analytic pieces of positive length are included.

7. CONCLUSION

Taxicab circular inversion $I_T(O,r)$ maps taxicab circles to piecewise-quadratic curves made of line segments, parabolic arcs, and, in the exceptional unbounded case, two rays. Concentric circles remain taxicab circles. For a nonconcentric source circle, the closed-versus-open character of the image is governed solely by $\rho = D = d_T(O,M)$: if the source circle avoids O, the inverse is closed and bounded; if it passes through O, the inverse is open and has two rays. A supporting line through O does not create unboundedness unless the corresponding finite source segment actually contains O.

The classification was derived directly from the coordinate formula for $I_T(O,r)$, the quadrantwise representation of the taxicab norm on vectors, and an edgewise analysis of the source circle. In general position, the three distance thresholds $\delta_1 = b, \delta_2 = a$, and $D = a + b$ are supplemented by the algebraic threshold Δ=a-b. Generic cases, axis contacts, passage through the inversion center, and the degeneration of a parabolic arc into a finite line segment are therefore described within one coherent framework.

The global implicit equation, the edgewise quadratic relations, and the complete threshold classification provide a reliable foundation for further work on smoothness, tangency, and curvature at junction points; invariant curves; pencils of taxicab circles; and analogous inversion classes in other polyhedral normed planes.

REFERENCES

Akça, Z., & Çalış, C. (2021). On the Voronoi diagram and taxicab plane. *Erzincan University Journal of Science and Technology, 14*(1), 175–181.

Akça, Z., & Kaya, R. (1997). On the taxicab trigonometry. *Journal of the Institute of Mathematics and Computer Sciences, Mathematics Series, 10*(3), 151–159.

Akça, Z., & Kaya, R. (2004a). On the distance formulae in three-dimensional taxicab space. *Hadronic Journal, 27*(5), 521–532.

Akça, Z., & Kaya, R. (2004b). On the norm in higher-dimensional taxicab spaces. *Hadronic Journal Supplement, 19*, 491–502.

Aydın, S. A. (2023). *On fractals and circular inversions* [Master's thesis, Eskişehir Osmangazi University].

Bayar, A., & Aydın, S. A. (2024). On taxicab circle inverses of lines. *Ikonion Journal of Mathematics, 6*(1), 1–8.

Bayar, A., & Ekmekçi, S. (2014). On circular inversions in taxicab plane. *Journal of Advanced Research in Pure Mathematics, 6*(4), 33–39.

Blair, D. E. (2000). *Inversion theory and conformal mapping*. American Mathematical Society.

Cırık, Y., & Ekmekçi, S. (2022). On the maximum spherical inversions. *Erzincan University Journal of Science and Technology, 15*(1), 360–371.

Ekmekçi, S. (2023a). A note on the maximum circle inverses of lines in the maximum plane. *Ikonion Journal of Mathematics, 5*(2), 1–9.

Ekmekçi, S. (2023b). On the maximum circular inverses of maximum circles. *Eskişehir Technical University Journal of Science and Technology A: Applied Sciences and Engineering, 24*(4), 324–335.

Krause, E. F. (1975). *Taxicab geometry: An adventure in non-Euclidean geometry*. Addison-Wesley.

Nickel, J. A. (1995). A budget of inversion. *Mathematical and Computer Modelling, 21*(6), 87–93.

Ramirez, J. L., Rubiano, G. N., & Jurčič-Zlobec, B. (2015). Generating fractal patterns by using p-circle inversion. *Fractals, 23*(4), 1550047.

Schattschneider, D. J. (1984). The taxicab group. *The American Mathematical Monthly, 91*(7), 423–428.

Yüca, G., & Can, Z. (2020). On the circular inversion in maximum plane. *Ikonion Journal of Mathematics, 2*(2), 26–34.

Advancements in Research on Doped Photocatalysts for Environmental Application

Nazlı TÜRKTEN[*1]

Yunus KARATAŞ[1]

[1]Department of Chemistry/Faculty of Arts and Sciences, Kirsehir Ahi Evran University, Türkiye
[*](nazli.turkten@ahievran.edu.tr) Email of the corresponding author

ABSTRACT

Nowadays, water pollution has emerged as a global issue due to rapid industrial development and the discharge of untreated industrial wastewater containing a wide diversity of organic, inorganic, and microbial effluents. The presence of toxic and carcinogenic compounds in water resources can have detrimental impacts on human health and aquatic life. Therefore, the application of effective wastewater treatment to comply with environmental regulations that contain several stringent norms set by governments is essential. Heterogeneous photocatalysis is a popular advanced oxidation technology for eliminating persistent compounds. Photocatalysis using semiconductors, such as TiO_2 and ZnO, is preferred for its affordability, non-toxicity, and strong oxidative capability. However, the wide band gap of these popular semiconductor metal oxides limits their use under visible light. The doping procedure is an effective strategy for preparing visible-light-active photocatalysts using non-metal dopants and metal dopants (transition metals and noble metals), and it can also improve photocatalytic performance by narrowing the band gap. Numerous studies have focused on designing novel doped photocatalysts and identifying appropriate dopants with their optimal amounts to enhance photocatalytic activity in the visible region by facilitating electron-hole separation. This mini-review is valuable to readers as it explores all aspects of the doping approach and photocatalysis, as well as future directions and limitations.

Keywords – Doping, doped TiO_2, heterogeneous photocatalysis, photocatalyst, photocatalytic degradation, water treatment.

I. INTRODUCTION

The decline in water quality standards for wastewater treatment is a major issue, leading to a variety of pollutants in water resources. The disposal of insufficiently treated wastewater, particularly from textile, pharmaceutical, and printing industries, commonly contains dyes, chemical precursors, and nitro compounds. Moreover, water containing dyes or hazardous effluents can significantly decrease soil fertility. Thus, sustainable treatment is essential to overcome critical environmental problems that can cause health problems for humans and harm to aquatic life [1-6].

Ozonation, electrochemical processes, direct water decomposition, and photocatalysis are advanced oxidation process technologies that rely on the formation of hydroxyl radicals. Ozonation is the process of directly injecting ozone gas into wastewater, where it reacts with organic pollutants or hydroxyl radicals, leading to indirect oxidative decomposition. Fenton treatment produces hydroxyl radicals through the decomposition of H_2O_2 with Fe^{2+} in an aqueous solution. This reaction occurs at pH levels below 4, and adjusting the pH increases operational costs. Direct water decomposition

treatment contains microwaves, ultrasound, and electromagnetic beams [7-10].

Heterogeneous photocatalysis is an environmentally friendly method that uses semiconductor metal oxides to eliminate a wide range of recalcitrant pollutants without causing secondary pollution. In this method, the process begins with the activation of the excited photocatalyst surface under UV light, which possesses photon energy equal to or greater than its band gap energy. The process of exciting an electron from the valence band to the conduction band leads to the formation of electron-hole pairs. These pairs can react with water, oxygen molecules, or hydroxyl groups to produce highly reactive oxygen species, such as superoxide anions and hydroxyl radicals. After that, the oxidation reactions take place as these radicals attack and degrade organic pollutants. Among semiconductors, TiO_2 and ZnO are the most studied and popular metal oxides due to their affordability, non-toxicity, and high oxidation capabilities. However, their wide band energies (~3,2 eV) limit their utilization under visible light and increase electron-hole recombination, negatively affecting photocatalytic efficiency. [4, 7, 11-13].

II. DOPING STRATEGY

Recent modification strategies on doped TiO_2 and doped ZnO have been conducted to narrow their band gaps and improve their photocatalytic reactivity under visible light [7, 14-17]. In this context, doping is a practical technique performed by incorporating a guest atom using non-metal elements (carbon, nitrogen, boron, sulphur, fluorine, iodine, etc.), metal elements (iron, manganese, copper, etc.), and noble metals (platinum, silver, gold, etc.) into the structure of the host semiconductor [7, 15, 18-20].

The dopants are applied to modify the electronic structure of semiconductors, retarding charge recombination, creating defect sites in the band gap, and broadening their operational range from ultraviolet to visible light. In the first situation, the recombination of charge carriers is hindered, and interfacial charge transfer is improved due to the trapping of holes from the valence band or electrons from the conduction band at defect sites. The second situation involves electronic transitions from defect states to the conduction band, or from the valence band to defect states, which are allowed under sub-band gap irradiation [7, 15, 21].

Research on non-metal dopants such as carbon, phosphorus, and sulfur has reported promising results for enhancing visible-light activity in TiO_2. Nitrogen can be incorporated into the TiO_2 structure easily, either in the bulk or as a surface dopant, due to its comparable atomic size to oxygen, low ionization energy, and high stability. The combination of metal dopants can significantly enhance photocatalytic lifespan and efficiency. Modifying TiO_2 with transition metals enhances its spectral response to the visible region and increases photocatalytic activity [19, 22-25]. The synergistic effects of various co-dopant ions play a key role in the decomposition of organic

pollutants in water and wastewater. Co-doping with multiple dopants addresses limitations by passivating impurity bands, reducing recombination center formation, enhancing dopant solubility parameters, and adjusting charge equilibrium [23, 26].

Recently, many studies have been conducted on doped TiO_2 photocatalysts that utilize both metals and non-metals [27-34]. Yalcin et al. prepared a series of single-doped TiO_2 photocatalysts containing non-metal dopants (nitrogen, sulfur, and carbon elements) through an incipient wet impregnation process [34]. The authors investigated the effects of dopants on the electronic and structural properties of TiO_2 using both experimental and computational methods. They reported that the photocatalytic activity for degrading 4-nitrophenol (4-NP) was significantly higher compared to undoped TiO_2. The iron-doped TiO_2 photocatalyst was synthesized by wet impregnation, which introduced additional electronic levels within the semiconductor's band gap due to iron doping [33]. In another photocatalytic study, the photocatalytic activities of nitrogen-, sulfur-, carbon-, and sulphur/nitrogen-codoped TiO_2 [30], iron-doped TiO_2 [31], and copper-doped TiO_2 [35] specimens were investigated on the degradation of humic acid. Gurkan et al. synthesized selenium/nitrogen codoped TiO_2 photocatalysts using $SeCl_4$ and urea as the dopant sources. The study revealed that co-doping of selenium/nitrogen anions in TiO_2 decreases the band gap by mixing N 2p with O 2p orbitals in the valence band and also introduces additional electronic states from the Se 3p orbitals within the band gap [29]. Additionally, a computational study was performed using first-principles density functional theory nitrogen-, carbon-, and sulphur-doped ZnO [36]. Sulphur-doped ZnO [37], manganese-doped ZnO [38], copper-doped ZnO [39], nitrogen-doped ZnO [40], and carbon/nitrogen codoped ZnO [41] were also prepared via different methods. Selected examples of doped photocatalysts are presented in Table 1.

Table 1. Selected Doped Photocatalysts used in Heterogeneous Photocatalysis

Photocatalyst Type	**Preparation Method**	**Pollutant**	**Ref.**
Selenium-doped TiO_2	wet impregnation method	4-NP	[27]
Iron-doped TiO_2	wet impregnation method	4-NP	[33]
Iron-doped TiO_2	wet impregnation method	humic acid	[31]
Copper-doped TiO_2	wet impregnation method	humic acid	[35]
Nitrogen-doped TiO_2	wet impregnation method	cefazolin	[28]
Nitrogen, Carbon, and Sulphur doped TiO_2	wet impregnation method	4-NP	[34]
Selenium/nitrogen codoped TiO_2	wet impregnation method	4-NP	[29]
Sulphur-doped ZnO	hydrothermal method	rhodamine B	[37]
Manganese-doped ZnO	wet-chemical method	basic aniline dye, methylene blue	[38]

Copper-doped ZnO	vapor transport method	resazurin	[39]
Carbon/nitrogen codoped ZnO	solvent-free mechano-thermal method	methylene blue, brilliant cresyl blue	[41]

III. CONCLUSION

This review study examines strategies for preparing cost-effective and sustainable photocatalysts designed to degrade persistent organic pollutants in water. Doping is an effective strategy for designing visible light photocatalysts and enhancing their photocatalytic activity. This can be achieved by using metal, non-metal, codopants, or multiple dopants. The addition of a dopant alters the electronic structure of the semiconductor, reduces the bandgap, and improves charge carrier separation. Advancements and collaborative efforts in various fields suggest that doping photocatalysts with metal and non-metal elements could significantly reduce the recombination rate of photogenerated electrons and holes. This improvement can lead to the development of visible-light-absorbing photocatalysts that address some of the most pressing environmental and energy challenges we face today.

REFERENCES

[1] A. Haleem, A. Shafiq, S.-Q. Chen, M. Nazar, A Comprehensive Review on Adsorption, Photocatalytic and Chemical Degradation of Dyes and Nitro-Compounds over Different Kinds of Porous and Composite Materials, Molecules, 28 (2023) 1081.

[2] A. Krishnan, A. Swarnalal, D. Das, M. Krishnan, V.S. Saji, S.M.A. Shibli, A review on transition metal oxides based photocatalysts for degradation of synthetic organic pollutants, J. Environ. Sci., 139 (2024) 389–417.

[3] A. Kumar, G. Sharma, M. Naushad, A.a.H. Al-Muhtaseb, A. García-Peñas, G.T. Mola, C. Si, F.J. Stadler, Bio-inspired and biomaterials-based hybrid photocatalysts for environmental detoxification: A review, Chem. Eng. J., 382 (2020) 122937.

[4] H. Kumari, Sonia, Suman, R. Ranga, S. Chahal, S. Devi, S. Sharma, S. Kumar, P. Kumar, S. Kumar, A. Kumar, R. Parmar, A Review on Photocatalysis Used For Wastewater Treatment: Dye Degradation, Water, Air, & Soil Pollution, 234 (2023) 349.

[5] M. Motamedi, L. Yerushalmi, F. Haghighat, Z. Chen, Recent developments in photocatalysis of industrial effluents : A review and example of phenolic compounds degradation, Chemosphere, 296 (2022) 133688.

[6] M. Ahtasham Iqbal, S. Akram, S. khalid, B. Lal, S.U. Hassan, R. Ashraf, G. Kezembayeva, M. Mushtaq, N. Chinibayeva, A. Hosseini-Bandegharaei, Advanced photocatalysis as a viable and sustainable wastewater treatment process: A comprehensive review, Environ. Res., 253 (2024) 118947.

[7] M.R.D. Khaki, M.S. Shafeeyan, A.A.A. Raman, W.M.A.W. Daud, Application of doped photocatalysts for organic pollutant degradation - A review, Journal of Environmental Management, 198 (2017) 78–94.

[8] L. Liu, Z. Chen, J. Zhang, D. Shan, Y. Wu, L. Bai, B. Wang, Treatment of industrial dye wastewater and pharmaceutical residue wastewater by advanced oxidation processes and its combination with nanocatalysts: A review, J. Water Process. Eng., 42 (2021) 102122.
[9] D. Ma, H. Yi, C. Lai, X. Liu, X. Huo, Z. An, L. Li, Y. Fu, B. Li, M. Zhang, L. Qin, S. Liu, L. Yang, Critical review of advanced oxidation processes in organic wastewater treatment, Chemosphere, 275 (2021) 130104.
[10] A.M. Mohammed, F. Aziz, S.S. Mohtar, S.A. Mhamad, B. Ahmadu, M.U. Nasir, K.Y. Muhammad, M. Aziz, A review of research trends on the usage of photocatalysis for wastewater treatment: bibliometric analysis, Sustainable Water Resources Management, 9 (2023) 88.
[11] N.R. Khalid, A. Majid, M.B. Tahir, N.A. Niaz, S. Khalid, Carbonaceous-TiO_2 nanomaterials for photocatalytic degradation of pollutants: A review, Ceram. Int., 43 (2017) 14552–14571.
[12] E. Kusmierek, A CeO_2 Semiconductor as a Photocatalytic and Photoelectrocatalytic Material for the Remediation of Pollutants in Industrial Wastewater: A Review, Catalysts, 10 (2020) 1435.
[13] A.S. Morshedy, E.M. El-Fawal, T. Zaki, A.A. El-Zahhar, M.M. Alghamdi, A.M.A. El Naggar, A review on heterogeneous photocatalytic materials: Mechanism, perspectives, and environmental and energy sustainability applications, Inorg. Chem. Commun., 163 (2024) 112307.
[14] W. Fang, M. Xing, J. Zhang, Modifications on reduced titanium dioxide photocatalysts: A review, J. Photochem. Photobiol. C: Photochem. Rev., 32 (2017) 21–39.
[15] M.A. Henderson, A surface science perspective on TiO_2 photocatalysis, Surf. Sci. Rep., 66 (2011) 185–297.
[16] L. Hua, Z. Yin, S. Cao, Recent Advances in Synthesis and Applications of Carbon-Doped TiO_2 Nanomaterials, Catalysts, 10 (2020) 1431.
[17] K.M. Lee, C.W. Lai, K.S. Ngai, J.C. Juan, Recent developments of zinc oxide based photocatalyst in water treatment technology: A review, Water Res., 88 (2016) 428–448.
[18] R.S.R. Mohd Zaki, R. Jusoh, I. Chanakaewsomboon, H.D. Setiabudi, Recent advances in metal oxide photocatalysts for photocatalytic degradation of organic pollutants: A review on photocatalysts modification strategies, Materials Today: Proceedings, 107 (2024) 59–67.
[19] M. Pelaez, N.T. Nolan, S.C. Pillai, M.K. Seery, P. Falaras, A.G. Kontos, P.S.M. Dunlop, J.W.J. Hamilton, J.A. Byrne, K. O'Shea, M.H. Entezari, D.D. Dionysiou, A review on the visible light active titanium dioxide photocatalysts for environmental applications, Appl. Catal. B, 125 (2012) 331–349.
[20] F. Kanwal, T. Javed, F. Hussain, M. Wasim, M. Batool, Enhanced dye photodegradation through ZnO and ZnO-based photocatalysts doped with selective transition metals: a review, Environmental Technology Reviews, 13 (2024) 754–793.
[21] H. Park, Y. Park, W. Kim, W. Choi, Surface modification of TiO_2 photocatalyst for environmental applications, J. Photochem. Photobiol. C: Photochem. Rev., 15 (2013) 1–20.
[22] N. Li, J. Ma, Y. Zhang, L. Zhang, T. Jiao, Recent Developments in Functional Nanocomposite Photocatalysts for Wastewater Treatment: A Review, Advanced Sustainable Systems, 6 (2022) 2200106.

[23] A. Piątkowska, M. Janus, K. Szymański, S. Mozia, C-,N- and S-Doped TiO_2 Photocatalysts: A Review, Catalysts, 11 (2021) 144.
[24] N. Puri, A. Gupta, Water remediation using titanium and zinc oxide nanomaterials through disinfection and photo catalysis process: A review, Environ. Res., 227 (2023) 115786.
[25] S. Rehman, R. Ullah, A.M. Butt, N.D. Gohar, Strategies of making TiO_2 and ZnO visible light active, J. Hazard. Mater., 170 (2009) 560–569.
[26] S.S. Mohtar, F. Aziz, A.F. Ismail, N.S. Sambudi, H. Abdullah, A.N. Rosli, B. Ohtani, Impact of Doping and Additive Applications on Photocatalyst Textural Properties in Removing Organic Pollutants: A Review, Catalysts, 11 (2021) 1160.
[27] Y.Y. Gurkan, E. Kasapbasi, Z. Cinar, Enhanced solar photocatalytic activity of TiO_2 by selenium(IV) ion-doping: Characterization and DFT modeling of the surface, Chem. Eng. J., 214 (2013) 34–44.
[28] Y.Y. Gurkan, N. Turkten, A. Hatipoglu, Z. Cinar, Photocatalytic degradation of cefazolin over N-doped TiO_2 under UV and sunlight irradiation: Prediction of the reaction paths via conceptual DFT, Chem. Eng. J., 184 (2012) 113–124.
[29] Y. Gurkan, E. Kasapbasi, N. Turkten, Z. Cinar, Influence of Se/N Codoping on the Structural, Optical, Electronic and Photocatalytic Properties of TiO_2, Molecules, 22 (2017) 414.
[30] C. Birben Nazmiye, S. Uyguner-Demirel Ceyda, S. Sen-Kavurmaci, Y. Gürkan Yelda, N. Türkten, M. Kılıç, Z. Çınar, M. Bekbolet, Photocatalytic Performance of Anion Doped TiO2 on the Degradation of Complex Organic Matrix, Journal of Advanced Oxidation Technologies, 2016, pp. 199.
[31] N.C. Birben, C.S. Uyguner-Demirel, S.S. Kavurmaci, Y.Y. Gürkan, N. Turkten, Z. Cinar, M. Bekbolet, Application of Fe-doped TiO_2 specimens for the solar photocatalytic degradation of humic acid, Catal. Today, 281 (2017) 78–84.
[32] N.C. Birben, C.S. Uyguner-Demirel, S. Sen-Kavurmaci, Y.Y. Gurkan, N. Turkten, Z. Cinar, M. Bekbolet, Comparative evaluation of anion doped photocatalysts on the mineralization and decolorization of natural organic matter, Catal. Today, 240, Part A (2015) 125–131.
[33] Y. Yalçın, M. Kılıç, Z. Çınar, Fe^{+3}-doped TiO_2: A combined experimental and computational approach to the evaluation of visible light activity, Appl. Catal. B, 99 (2010) 469–477.
[34] Y. Yalçın, M. Kılıç, Z. Çınar, The Role of Non-Metal Doping in TiO_2 Photocatalysis, Journal of Advanced Oxidation Technologies, 13 (2010) 281–296.
[35] N. Turkten, Z. Cinar, A. Tomruk, M. Bekbolet, Copper-doped TiO_2 photocatalysts: application to drinking water by humic matter degradation, Environ Sci Pollut Res Int, 26 (2019) 36096–36106.
[36] W. Yu, J. Zhang, T. Peng, New insight into the enhanced photocatalytic activity of N-, C- and S-doped ZnO photocatalysts, Appl. Catal. B, 181 (2016) 220–227.
[37] Z. Mirzaeifard, Z. Shariatinia, M. Jourshabani, S.M. Rezaei Darvishi, ZnO Photocatalyst Revisited: Effective Photocatalytic Degradation of Emerging Contaminants Using S-Doped ZnO Nanoparticles under Visible Light Radiation, Industrial & Engineering Chemistry Research, 59 (2020) 15894–15911.
[38] R. Ullah, J. Dutta, Photocatalytic degradation of organic dyes with manganese-doped ZnO nanoparticles, J. Hazard. Mater., 156 (2008) 194–200.
[39] R. Mohan, K. Krishnamoorthy, S.-J. Kim, Enhanced photocatalytic activity of Cu-doped ZnO nanorods, Solid State Commun., 152 (2012) 375–380.

[40] H. Qin, W. Li, Y. Xia, T. He, Photocatalytic Activity of Heterostructures Based on ZnO and N-Doped ZnO, ACS Applied Materials & Interfaces, 3 (2011) 3152–3156.
[41] P.L. Meena, A.K. Surela, L.K. Chhachhia, J. Meena, R. Meena, Investigation of the photocatalytic potential of C/N-co-doped ZnO nanorods produced via a mechano-thermal process, Nanoscale Advances, 7 (2025) 1335–1352.

The Predicted Toxicity Profiles of Four Commercial Textile Dyes

Nazlı TÜRKTEN[*1]

Yunus KARATAŞ[1]

[1]Department of Chemistry/Faculty of Arts and Sciences, Kirsehir Ahi Evran University, Türkiye
[*](nazli.turkten@ahievran.edu.tr) Email of the corresponding author

ABSTRACT

Conventional textile dyeing and printing methods can often threaten ecological sustainability and human health due to significant environmental pollution, excessive water usage, and the release of auxiliaries and metal ions. The coloring process primarily uses chemical dyeing techniques with traditional colorants, applying dyes or pigments to form colored fibers through chemical bonds or physical adsorption. Azo disperse dyes have been the most widely used synthetic dyes among disperse dyes in the past decade. Their popularity can be attributed to the ease of manufacturing and their diverse applications in cosmetics, textile dyeing, and printing. The disperse dyes were originally designed for cellulose acetate fibers, but the recent dominance of poly(ethylene terephthalate) (PET) in the market has led to modifications in their structure to enhance compatibility with PET dye systems. Several disperse dyes are still believed to be the most common causes of textile-related allergic contact dermatitis; however, there is limited data regarding their current usage in textiles. These dyes do not form a chemical bond with the fibers of the fabric due to their small, lipophilic molecules, which can easily transfer onto the skin of the person wearing the garment. In this study, the toxicity risk assessments of four commercial dyes, Disperse Blue 60 (DB-60), Disperse Orange 37 (DO-37), Disperse Red 1 (DR-1), and Disperse Yellow 3 (DY-3), were evaluated by the ProTox 3.0 *in silico* tool. The predicted median lethal dose (LD_{50}) values varied considerably among the selected dyes, ranging from 33 mg/kg for DB-60 to 3200 mg/kg for DO-37.

Keywords – Disperse Blue 60, Disperse Orange 37, Disperse Red 1, Disperse Yellow 3, in silico, ProTox 3.0, Toxicity.

I. INTRODUCTION

Disperse dyes are specifically used to dye synthetic fabrics made from fibers that are entirely polyester, acetate, or nylon, as well as blends of these materials with other fiber types. Conversely, these synthetic colorants are not effective on natural fibers such as wool, cotton, and linen. Disperse dyes do not form a chemical bond with the fibers, and this is particularly likely to occur if the textile has poor fastness. Furthermore, these hydrophobic dyes can be removed through rubbing or exposure to water. Additionally, these dyes are known mostly as allergenic dyes because of their low molecular weight and lipophilic properties. [1-4].

PET is a popular hydrophobic fiber known for its wrinkle resistance, excellent washability, and abrasion resistance. The dyeing procedure of this fabric primarily involves water dyeing with disperse dyes at high temperatures and pressures. Despite their low water solubility, disperse azo dyes are dispersed in water with surfactants such as sulfonated lignin, which are essential components in commercial dyeing formulations. It is reported that

approximately 60% of all disperse dyes are azo dyes, while about 25% are anthraquinone dyes. The remaining types of disperse dyes include quinophthalone, methine, naphthalimide, naphthoquinone, and nitro dyes. Azo disperse dyes are commonly used in textile dyeing to produce nearly the entire spectrum of shade due to their low cost and ease of application, making them the most utilized class of dyes. Although it is estimated that approximately 100,000 tons of azo disperse dyes are supplied annually, there is limited data available regarding their ecotoxicity. The persistent characteristics of disperse dyes under end-use conditions make them ideal for coloring textiles. However, improperly treated wastewater can lead to environmental issues and harm aquatic life if they are discharged directly. Therefore, it is essential to assess the toxicological risks associated with disperse dyes [1-3, 5-7].

This study aimed to comparatively evaluate the predicted acute toxicity, toxicity endpoints, and organ-specific toxicity profiles of four commercially relevant disperse dyes using an *in silico* approach with ProTox.

II. Materials and Method

The predicted toxicological assessments for four commercial disperse dyes were calculated via an *in silico* tool (https://tox.charite.de/protox3/), ProTox 3.0. [8]. This open-source platform utilizes machine learning algorithms to predict toxicity and associated endpoints. Additional information about this computational method was provided in our previous study [9]. The chemical structures of the selected four disperse dyes are presented in Figure 1.

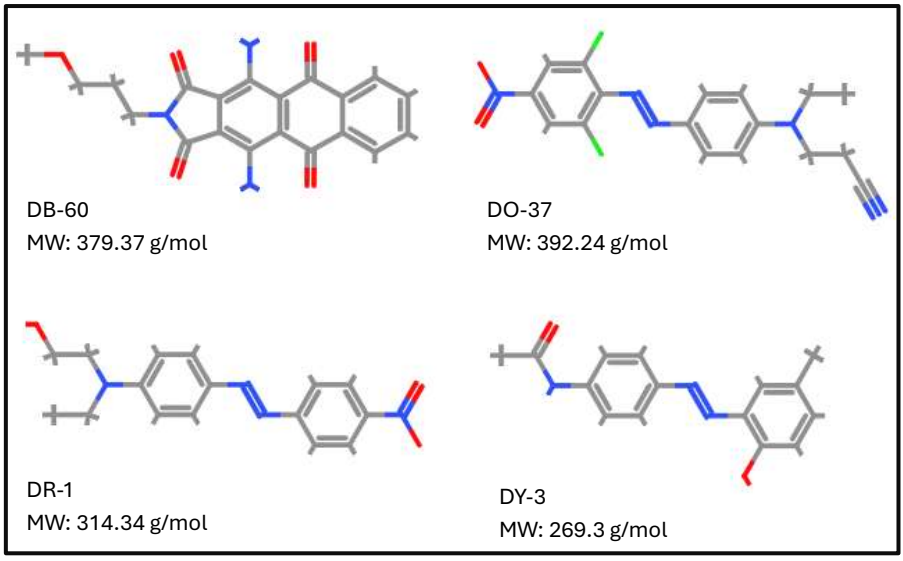

Fig. 1 Molecular structures of DB-60, DO-37, DR-1, and DY-3 dyes. Atom colors: blue: nitrogen, gray: carbon, green: chlorine, red: oxygen atoms.

III. RESULTS

The determined LD_{50} values and the calculated toxicological classes of the disperse dyes DB-60, DO-37, DR-1, and DY-3 are presented in Table 1.

Table 1. The predicted LD_{50} values and toxicological class of DB-60, DO-37, DR-1, and DY-3 disperse dyes

Specimens	Predicted LD_{50} mg/kg	Predicted Toxicity Class	Prediction accuracy %
DB-60	33	2	67.4
DO-37	3200	5	69.3
DR-1	760	4	68.1
DY-3	810	4	100.0

The LD_{50} value calculated for DB-60 is 33 mg/kg, classifying it as fatal if swallowed (class 2), while DO-37 is 3200 mg/kg, indicating that it may be harmful if swallowed (class 5). DR-1 and DY-3 disperse dyes are classified as toxicity class 4, indicating they may be harmful if swallowed. Among the four dyes, DB-60 exhibited the highest predicted acute oral toxicity, with an LD_{50} of 33 mg/kg and assignment to toxicity class 2. Its predicted LD_{50} was approximately 97-fold lower than that of DO-37, indicating a marked difference in acute toxicity potential among the disperse dyes investigated.

The toxicological results of the disperse dyes DB-60, DO-37, DR-1, and DY-3, including their toxicity endpoints and organ toxicity features, are summarized in Table 2. Toxicity radar plots are used to compare the toxicity properties of the dyes (Figure 2).

Table 2. The predicted toxicity endpoints and organ toxicity profiles of DB-60, DO-37, DR-1, and DY-3 disperse dyes

Toxicity endpoints								
Specimens	Immunotoxicity	Mutagenicity	Cytotoxicity	Blood–brain barrier (BBB)	Ecotoxicity	Clinical toxicity	Nutritional toxicity	Carcinogenicity
DB-60	Inactive	Inactive	Active	Active	Inactive	Active	Inactive	Active
DO-37	Inactive	Active	Inactive	Active	Active	Inactive	Inactive	Active
DR-1	Inactive	Active	Inactive	Active	Active	Inactive	Inactive	Active
DY-3	Inactive	Active	Inactive	Active	Active	Active	Inactive	Active

Organ Toxicity					
Specimens	**Hepatotoxicity**	**Neurotoxicity**	**Nephrotoxicity**	**Cardiotoxicity**	**Respiratory toxicity**
DB-60	Inactive	Active	Active	Inactive	Active
DO-37	Inactive	Active	Inactive	Inactive	Active
DR-1	Inactive	Inactive	Inactive	Inactive	Active
DY-3	Active	Active	Inactive	Inactive	Inactive

All four dyes were predicted to be active for BBB-related toxicity and carcinogenicity endpoints. Mutagenicity was predicted for DO-37, DR-1, and DY-3, whereas DB-60 showed a distinct profile characterized by predicted cytotoxicity and nephrotoxicity. Among the investigated dyes, DY-3 was the only compound predicted to exhibit hepatotoxicity.

The phytotoxicity assay with *Raphanus sativus* L. seeds confirmed that the products resulting from dye decolorization are nontoxic, in contrast to the high toxicity of DB-60 dye observed in radish seeds [10]. It was reported that high mutagenic activity was observed in the *Salmonella/*microsome assay, particularly with the mutagenic nitro-aminoazobenzene dye DO-37 and benzidine, a known carcinogen [11]. This outcome is consistent with the predictions made through *in silico* analysis.

The toxic and genotoxic effects of DR-1 disperse dye on sexually mature male mice (*Mus musculus*, strain CF-1) were reported, and the results revealed the harmful activity of this commercial dye on reproductive health [12]. In another toxicological study, the mutagenicity of DR-1 dye was tested on *Salmonella* assay, and it was found to be positive [13]. Moreover, DR-1 was reported as highly toxic to *Daphnia similis* with an EC_{50} (median effective concentration) value of 127 μg/L [14]. The toxicity of the DY-3 dye was tested on the strain YG1041, revealing a potency with S9 of 5.5 rev μ/g [15].

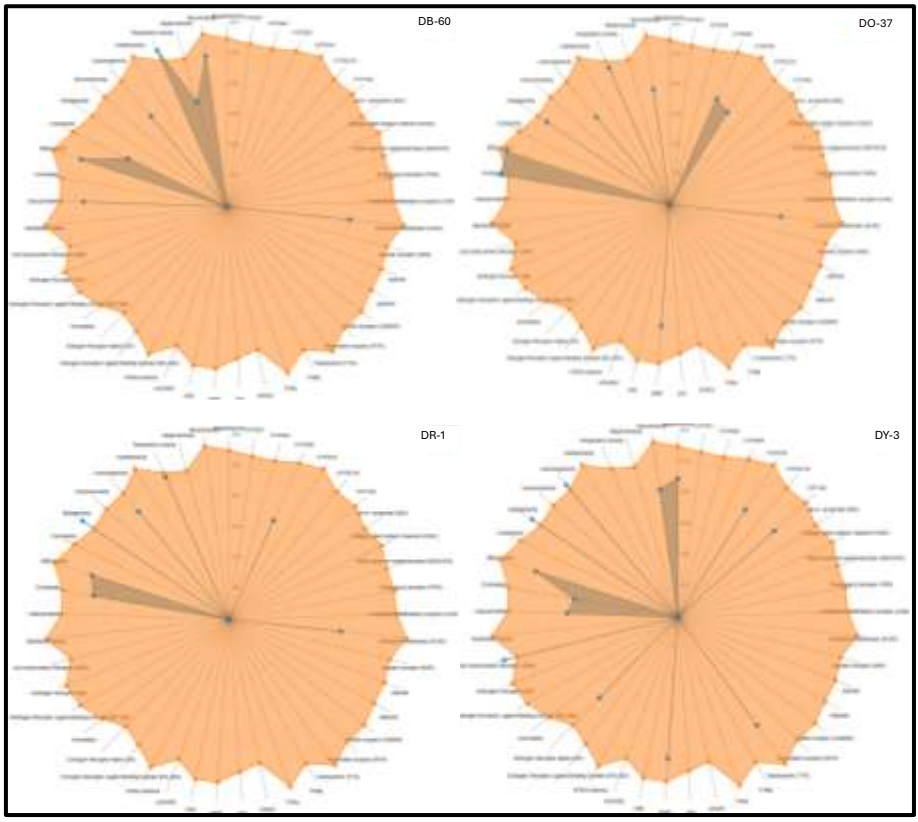

Fig. 2 Toxicity radar plots of DB-60, DO-37, DR-1, and DY-3 dyes.

IV. CONCLUSION

The predicted toxicity profile of four commercial dyes, DB-60, DO-37, DR-1, and DY-3 via *in silico* ProTox 3.0 platform was investigated. The LD_{50} values of DB-60, DO-37, DR-1, and DY-3 dyes were found to be 33 mg/kg, 3200 mg/kg, 760 mg/kg, and 810 mg/kg, respectively. DB-60 was assigned to toxicity class 2, indicating substantially higher predicted acute oral toxicity than DO-37, DR-1, and DY-3. Furthermore, carcinogenicity and BBB-related toxicity were predicted as active endpoints for all four dyes. These findings highlight the need for systematic hazard screening of disperse dyes and demonstrate the potential of in silico approaches for prioritizing compounds for further experimental toxicological assessment. Additionally, performing comprehensive evaluations of exposure and toxicity is essential for accurately assessing the health risks linked to these disperse dyes.

REFERENCES

[1] A.M. Al-Etaibi, M.A. El-Apasery, Facile Synthesis of Novel Disperse Dyes for Dyeing Polyester Fabrics: Demonstrating Their Potential Biological Activities, Polymers, 14 (2022) 3966.
[2] L. Malinauskiene, M. Bruze, K. Ryberg, E. Zimerson, M. Isaksson, Contact allergy from disperse dyes in textiles–a review, Contact Dermatitis, 68 (2013) 65–75.
[3] G.A. Umbuzeiro, M. Szymczyk, M. Li, Y. Chen, J.A.S. Vendemiatti, A.F. de Albuquerque, A. dos Santos, B.d.S. Maselli, F. Kummrow, N.R. Vinueza, H.S. Freeman, Purification and characterization of three commercial phenylazoaniline disperse dyes, Coloration Technology, 133 (2017) 513–518.
[4] S. Rahimi, M.P. Singh, J. Gupta, Adverse effects of textile dyes on antioxidant enzymes and cholinesterase activities in *Drosophila melanogaster* (Oregon R^{+}), Drug Chem. Toxicol., 45 (2022) 1131–1139.
[5] E.R.A. Ferraz, Z. Li, O. Boubriak, D.P. de Oliveira, Hepatotoxicity Assessment of the Azo Dyes Disperse Orange 1 (DO1), Disperse Red 1 (DR1,) and Disperse Red 13 (DR13) in HEPG2 Cells, Journal of Toxicology and Environmental Health, Part A, 75 (2012) 991–999.
[6] F.I. Vacchi, P.C. Von der Ohe, A.F.d. Albuquerque, J.A.d.S. Vendemiatti, C.C.J. Azevedo, J.G. Honório, B.F.d. Silva, M.V.B. Zanoni, T.B. Henry, A.J. Nogueira, G.d.A. Umbuzeiro, Occurrence and risk assessment of an azo dye – The case of Disperse Red 1, Chemosphere, 156 (2016) 95–100.
[7] I. Nishi, T. Yoshitomi, F. Nakano, H. Uemura, T. Kawakami, Identification of an aryl hydrocarbon receptor agonistic disperse dye in commercially available textile products by effect-directed analysis, Chemosphere, 375 (2025) 144247.
[8] N.G. Bakhtyari, G. Raitano, E. Benfenati, T. Martin, D. Young, Comparison of In Silico Models for Prediction of Mutagenicity, Journal of Environmental Science and Health, Part C, 31 (2013) 45–66.
[9] N. Turkten, Y. Karatas, S. Kurumoglu, Y. Yalcin Gurkan, Enhanced photocatalytic degradation of diazo reactive blue 198 using ternary PANI-TiO_2-CuO composites: Predicted degradation pathway, mechanism, and DFT calculations, Physica B: Condensed Matter, 717 (2025) 417802.
[10] Z.S. Seyedi, F. Jookar Kashi, Z. Zahraei, Isolation, characterization, and decolorization of Disperse Blue 60 by newly isolated bacterial strains from Kashan textile wastewater, Water Environ. Res, 92 (2020) 873–879.
[11] R.O. Alves de Lima, A.P. Bazo, D.M.F. Salvadori, C.M. Rech, D. de Palma Oliveira, G. de Aragão Umbuzeiro, Mutagenic and carcinogenic potential of a textile azo dye processing plant effluent that impacts a drinking water source, Mutation Research/Genetic Toxicology and Environmental Mutagenesis, 626 (2007) 53–60.
[12] F.H. Fernandes, E. Bustos-Obregon, D.M.F. Salvadori, Disperse Red 1 (textile dye) induces cytotoxic and genotoxic effects in mouse germ cells, Reproductive Toxicology, 53 (2015) 75–81.
[13] E.R.A. Ferraz, G.A. Umbuzeiro, G. de-Almeida, A. Caloto-Oliveira, F.M.D. Chequer, M.V.B. Zanoni, D.J. Dorta, D.P. Oliveira, Differential toxicity of Disperse Red 1 and Disperse Red 13 in the Ames test, HepG2 cytotoxicity assay, and Daphnia acute toxicity test, Environmental Toxicology, 26 (2011) 489–497.
[14] B. Singh, K. Bauddh, F. Bux, Algae and Environmental Sustainability, 2015.

[15] F.I. Vacchi, J.A.d.S. Vendemiatti, B.F. da Silva, M.V.B. Zanoni, G.d.A. Umbuzeiro, Quantifying the contribution of dyes to the mutagenicity of waters under the influence of textile activities, Sci. Total Environ., 601-602 (2017) 230–236.